Swansea University
Prifysgol Abertawe

Cronfa
Setting Research Free

Swansea University E-Theses

Computational blood flow studies on model and realistic geometries.

Yatishchandra, Yatishchandra

How to cite:

Yatishchandra, Yatishchandra (2010) *Computational blood flow studies on model and realistic geometries..* thesis, Swansea University.
http://cronfa.swan.ac.uk/Record/cronfa42411

Use policy:

This item is brought to you by Swansea University. Any person downloading material is agreeing to abide by the terms of the repository licence: copies of full text items may be used or reproduced in any format or medium, without prior permission for personal research or study, educational or non-commercial purposes only. The copyright for any work remains with the original author unless otherwise specified. The full-text must not be sold in any format or medium without the formal permission of the copyright holder. Permission for multiple reproductions should be obtained from the original author.

Authors are personally responsible for adhering to copyright and publisher restrictions when uploading content to the repository.

Please link to the metadata record in the Swansea University repository, Cronfa (link given in the citation reference above.)

http://www.swansea.ac.uk/library/researchsupport/ris-support/

Swansea University
Prifysgol Abertawe

Master of Philosphy Thesis

Computational Blood Flow Studies on Model and Realistic Geometries

by

Yatishchandra Y

Thesis submitted to the Swansea University in candidature for the degree of Master of Philosophy

Supervisors: Professor P Nithiarasu and Dr Igor Sazonov

SWANSEA UNIVERSITY
LIBRARY

R

NOT TO BE
REMOVED FROM
THE LIBRARY

Civil and Computational Engineering Centre
School of Engineering
Swansea University, Swansea
United Kingdom

June 2010

ProQuest Number: 10798119

All rights reserved

INFORMATION TO ALL USERS
The quality of this reproduction is dependent upon the quality of the copy submitted.

In the unlikely event that the author did not send a complete manuscript
and there are missing pages, these will be noted. Also, if material had to be removed,
a note will indicate the deletion.

ProQuest 10798119

Published by ProQuest LLC (2018). Copyright of the Dissertation is held by the Author.

All rights reserved.
This work is protected against unauthorized copying under Title 17, United States Code
Microform Edition © ProQuest LLC.

ProQuest LLC.
789 East Eisenhower Parkway
P.O. Box 1346
Ann Arbor, MI 48106 – 1346

UNIVERSITY OF WALES SWANSEA
LIBRARY

Abstract

Study of blood flow inside arteries is physiologically significant and computationally challenging. Vascular diseases are the leading causes of death worldwide. Since the geometry is characterized by twisted, bended, bifurcated, trifurcated and multi-branched structure, the numerical modeling of blood flow is highly complicated. Blood flow is also complex due to the unsteady (pulsatile), three dimensional and helical nature. The computational work in this thesis contains flow simulation of few idealistic models followed by a thorough numerical study of a realistic thoracic abdominal aorta. The three dimensional, viscous Navier Stokes equations are solved explicitly using characteristic based split (CBS) method for time discretization and standard Galerkin method for spatial discretization by imposing physiologically relevant boundary conditions. The artificial compressibility method, which is found to be efficient for biomedical flow problems, has also been discussed briefly. The velocity vectors, wall shear stress contours and pressure distribution plots presented in this thesis provide important insight into actual behavior of blood flow inside arteries. The meshes contain boundary layers for accurate calculation of wall shear stress. The idealistic models studied under steady conditions are straight and s-shaped arteries. All these idealistic models represent healthy arteries. For idealistic models, it is found that complex secondary flow, pressure drop and the WSS vary with change in geometrical configurations and flow rate. In addition to idealistic models, a realistic thoracic aorta with an aneurysm has been studied, by prescribing fully developed pulsatile wave form at the inlet and all four exits. The patient specific geometrical data of this thoracic aorta has been obtained with the aid of standard CT scans and processed by AMIRA to construct an initial mesh. In this realistic simulation, WSS is found to be low at the beginning of the cardiac cycle, increases to maximum at the peak flow rate and decreases rapidly as the velocity drops. This research work involving fluid dynamical studies in arteries concludes that hemodynamic quantities such as Oscillatory shear index (OSI), flow separation and reversal regions and blood pressure may play a vital role in pathogenesis of arterial anomalies. The Numerical models and the required CBS and velocity profile generation codes have been provided by the team.

Acknowledgement

No academic task can be accomplished without the support of supervisors, colleagues, parents and friends. Its a pleasure to thank the people who played vital role in this research work. I would like to thank my supervisor Prof P Nithiarasu for his constant guidance, motivation and support throughout my tenure in Swansea University. I am very thankful for all the resources he has provided, including CBS code and computing facilities. Secondly, I am very grateful to co-supervisor Dr Igor Sazonov, research associate Dr P Saksono and fellow graduate student Mr Rhodri Bevan, for providing me the methodologies to build and run CFD models. The mesh for the realistic aorta has been provided by Dr Igor Sazonov. Dr P Saksono has provided the CBS solver and 3D codes for velocity profile generation. Without Dr P Saksono's involvement, interest and guidance, this thesis would have never been made possible. Dr Igor Sazonov was of great help during difficult situations of modeling issues. I offer my special regards to Mr Rhodri Bevan, since he supported my research work right from the early days to concluding stage.

I would like to express my gratitude to prestigious Civil and Computation Engineering Center for accepting me as one of its researchers and providing me the state of art technical facilities. My gratitude also goes to Dr Jason W Jones, for guiding me to perform Volume and Surface Triangulations. I owe my deepest gratitude to my parents and friends in India, for supporting my study abroad effort. The staff of Swansea University played a significant part by facilitating accommodation, library and other academic resources. Lastly, I would like to thank all of my local and Welsh friends, who supported my stay in Swansea.

DECLARATION

This work has not previously been accepted in substance for any degree and is not being currently submitted in candidature for any degree.

Signed.....(candidate)
Date.....05.07.10.....

STATEMENT 1

This thesis is the result of my own investigation, except where otherwise stated. Other sources are acknowledged by footnotes giving explicit references. A bibliography is appended.

Signed.....(candidate)
Date.....05.07.10.....

STATEMENT 2

I hereby give consent for my thesis, if accepted, to be available for photocopying and for inter-library loan, and for the title and summary to be made available to outside organizations.

Signed.....(candidate)
Date.....05.07.10.....

Table of Contents

Nomenclature

x, y, z	Three coordinates
u, v, w	Velocities in three directions
ψ	A scalar variable
V	Velocity vector
u_{mean}	Mean velocity of blood flow in cm/s^2
∇	Divergence term
δ_{ij}	Kroneckar delta
P	Blood pressure in dynes/cm^2
f_i	Force vector
t	Time in seconds
p_x	Pressure in dynes/cm^2 at point x
v_x	Velocity in cm/s at point x
γ	Specific weight in dynes/cm^3
ρ	Blood density in dynes/cm^3
h	Height between two points in cm
F_L	Frictional loss in dynes/cm^2
E	Kinetic energy in joules
ω	Frequency of pulsatile flow in cycles per second
R	Radius of the artery in cm
R_c	Radius of curvature of the artery in cm
D	Diameter of the artery cm
μ	Dynamic viscosity of blood in Poise
ν	Kinematic viscosity of blood in cm$^2/s$

Q	Flow rate in cm^3/s
Re	Reynolds number of blood flow
De	Dean number of blood flow in bends
τ	Shear stress in dynes/cm^2 on arterial wall calculated analytically
τ_{wall}	Shear stress in dynes/cm^2 on arterial wall calculated numerically
τ_{ij}	Deviatoric stress in dynes/cm^2 on arterial wall
I	Identity matrix
n	Normal vector
T	Time period of oscillations
$\vec{\tau_w}^*$	Stress component acting opposite to the temporal mean shear stress
OSI	Oscillatory Shear Index of blood flow
$TAWSS$	Time averaged Wall shear stress in dynes/cm^2s
$WSSG$	Wall shear stress gradient dynes/cm^3
$\otimes$	Tensor product
V^T	Independent variable vector in generic Navier Stokes equations
F^T	Convective flux vector in generic Navier Stokes equations
G^T	Diffusive flux vector in generic Navier Stokes equations
U_i	Momentum in generic Navier Stokes equations
c	Speed of sound in cm/s
u_∞	Freestream velocity in cm/s
u^*	Nondimensionalised velocity
ρ^*	Nondimensionalised Density
x_i^*	Nondimensionalised coordinates
t^*	Nondimensionalised time
P^*	Nondimensionalised pressure
U^*	Nondimensionalised momentum
τ_{ij}^*	Nondimensionalised deviotaric stress
$\tilde{U}$	Intermediate momentum
L	Charecteristic length in cm

β	Artificial compressibility parameter
ϵ	A small constant used to calculate β
v_{conv}	Convective velocity
v_{diff}	Diffusive velocity
h_e	Local element size in cm
N	Shape functions
Ω	Variable representing the domain
$\mathbf{M}$	Mass matrix
$\mathbf{B}$	Strain matrix
l	Length of the artery in cm
r_{norm}	Normalised radius
R_i	Radius measured from an imaginary node
$K(t)$	Transient profile for generating unsteady velocity boundary conditions
B_i	Amplitude of the pulsatile blood flow
ω_i	Angular frequency of the pulsatile blood flow
ϕ_i	Phase angle of the ith harmonics
W^{*SUPG}	Streamline upwind petrov Galerkin weight

List of Figures

List of Tables

Chapter 1

Introduction

1.1 Significance of haemodynamics

Haemodynamical study is important mainly to two research communities. First one is vascular research community and the second is engineering research community. Fluid mechanical factors play a key role in the pathogenesis of vascular disorders such as arteriolosclerosis, atherosclerosis and thromboembolism. In arteries, the relationship between local velocity and stress patterns, and atherosclerotic lesions has been confirmed by many researchers [1, 2, 3, 4, 5]. According to *Bharadvaj et al* [1] arterial regions with low or oscillatory shear stress are vulnerable for atherosclerotic lesions formation. *Ku et al* [5] have studied the localization of atheromatous plaque due to low wall shear stress, directionally varying stresses and longer residence time of fluid particles. Atherosclerotic lesions are commonly found in regions where an unidirectional laminar flow is changing its path due to curvature and bifurcations [6]. Turbulence at the branched locations of arterioles can trigger cell damage. *Frangos et al* [4] have presented the combined responsibility of shear force and circumferential strain in localization of atherosclerotic lesions. Apart from atherosclerotic disorders, haemodynamical anomalies in aged and weakened arteries can produce local dilations known as aneurysms. When these aneurysms in an aorta grow beyond a critical dimension (generally 5 cm or more), surgical intervention is required in terms of stents, grafts and coils. Post-surgery haemodynamical study in such cases requires monitoring of drag forces on stents [8]. Stenosis and restenosis are also commonly occurring vascular pathologies. The severity of a stenosis can be judged by decrease in haemodynamical flow rate at a location distal to it [9]. Determining haemodynamical quantities such as the wall shear stress and oscillatory shear index with the help of *in vivo* studies is not precise. Over the past few decades, extensive numerical simulation of bio-fluids has taken place in the field of vascular research. However, it is important to note that, there is a portion of research community involved in *in vitro* experimental research. These experimental studies rely on laser doppler velocimetry (LDV) and particle tracking Velocimetry (PTV) to quantify haemodynamical velocity. In the present generation of cardiovascular research, computational study of haemodynamics is also known as *in silico* study. In this thesis, numerical simulation of biomechanical problems will be referred to as *in silico* studies.

The literature survey presented here forms the substantial part of thesis. Computationally, the primary objective of this research topic is to compute haemodynamical quantities in

idealistic and realistic geometries with the aid of characteristic based split method [13]. The secondary objective is to study the impact of haemodynamical factors on vascular well being.

1.2 Layout of the thesis

The work undertaken here is highly multidisciplinary in nature. An attempt has been made to include all the significant concepts essential for the simulation of vascular bio-fluids. The concepts covered in this thesis range from basic fluid mechanics of biofluids to advanced computational fluid dynamics. The essence and path of blood flow in human body has been explained in the next chapter. A brief explanation about types of vessels has been presented in the same introductory chapter followed by a short discussion on haemodynamical quantities. Structure of a blood vessel plays a noticeable role in haemodynamics, thus a paragraph on biological vascular structure has also been included in the next chapter, followed by a brief discussion on properties of blood. Understanding the output of a CFD code is essential to make a pragmatic judgement on haemodynamical behavior, thus a chapter (3) has been added to explain flow features. Governing equations of bio-fluids and an efficient solution scheme employed in the present work will be explained in Chapter 4. The actual description of the numerical work undertaken during the course starts from Chapter 5. A paradigm problem illustrating the flow through a straight artery with constant radius will be described in the Chapter 5. In order to classify the flow in arteries with geometrical irregularities, flow through a bend type artery has been presented in the Chapter 6. Impact of multiple bends on the haemodynamical flow can be apprehended by the Chapter 7. Chapter 8 elucidates the impact of curvature angle of the artery on the flow. A double bend type artery with higher curvature angles has been studied thoroughly in this chapter. In the Chapter 9, a realistic model of an aorta inflicted with thoracic aortic aneurysm has been presented. The distribution of oscillatory shear index and wall shear stress in the TAA will be discussed in this chapter. An attempt has also been made to understand the pathogenesis of aneurysm, with the aid of CFD. The thesis will be completed with the concluding remarks on the work undertaken, in the Chapter 10.

Chapter 2

An introduction to vascular biomechanics

2.1 An overview on haemodynamical circulation

There are two types of circulation, namely pulmonary and systemic. Pulmonary circulation occurs between the heart and the lungs in order to oxygenate the blood. Systemic circulation involves two way transportation of blood from heart to tissues and vice versa. Coronary circulation is part of the systemic circulation, in which oxygenated blood is carried to heart muscle myocardium to supply nutrients. Systemic circulation is larger as compared to the pulmonary. The heart contains four chambers namely, right atrium, right ventricle, left atrium and left ventricle. Lungs dispose carbon dioxide from the blood, in order to oxygenate it. Through pulmonary veins, oxygenated blood from lungs enters the left atrium chamber of the heart and subsequently to the left ventricle. The oxygenated blood from left ventricle is pumped with high pressure to aorta. The oxygenated blood from aorta is transported to tissues via arterioles and capillaries. This phase of systemic circulation ensures the adequate supply of nutrients to the tissues. The deoxygenated blood returns to the heart, by entering the right atrium chamber followed by right ventricle. It is very important to know that oxygenated blood flows in a network, which involves arteries, arterioles and capillaries. Similarly, deoxygenated blood flows in the network of capillaries, venules and veins. These facts can be clarified by referring to the Figure 2.1. For comprehensive understanding of haemodynamical circulation, readers are referred to [11]. The haemodynamical circulation is necessary for efficient tissue perfusion. The blood flowing in a vessel satisfies all three laws of conservation. Similar to any other fluid, the forces that act on blood are gravitational load and pressure gradient. The forces that resist the blood flow are viscous-shear forces. Turbulence can also cause this resistance. Unlike a flow in a straight tube, the critical Re of turbulence for an intricate blood circulation tree is not 2000. It can be as low as 200 [7] due to geometrical complexities. The combination of maximum velocity and lower viscosity can also induce turbulence, due to increase in Re. It is obvious that presence of turbulence inside lumen will increase the magnitude of wall shear stress. This higher shear stress is due to higher shear strain and higher friction on endothelium. Inside a blood vessel, if the pressure and velocity at a point are known, pressure and velocity at any point downstream can be calculated approximately using bernoulli's equation with some additional terms in the right hand side. These additional terms include rate of change of kinetic energy between two points and frictional loss [11]. The frictional loss is low for a large artery

such as aorta.

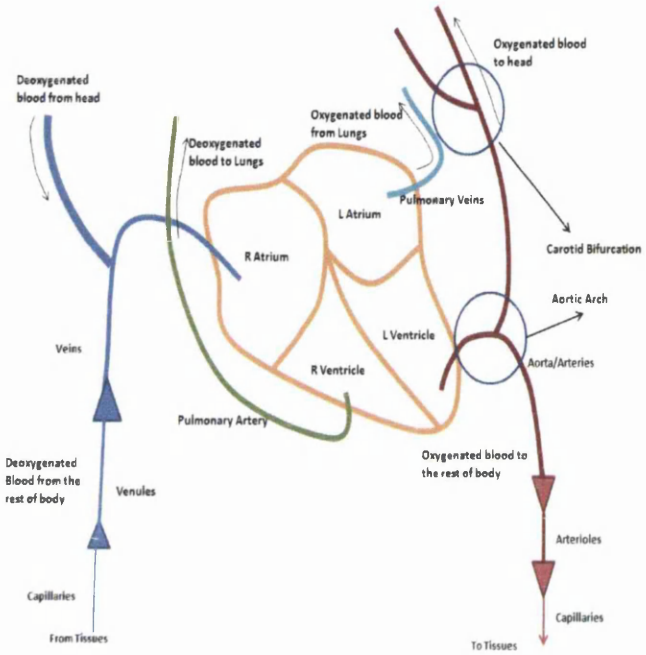

Figure 2.1: Blood circulation from human heart.

2.2 Haemodynamically important arteries

In the whole of circulation system, aorta is the biggest artery. The aorta is connected to the left ventricle of the heart and extends distal to the diaphragm. There are three sections in an aorta, namely ascending aorta, aortic arch and descending aorta. The arch of aorta branches into three arteries, namely brachycephalic artery, left common carotid artery and left subclavian artery. The aorta has always been a center of attraction for many researchers [8, 16, 17, 22] in haemodynamics, since it is susceptible to dilatations such as thoracic and abdominal aortic aneurysms. However, another most widely researched [1, 2, 3, 5] artery is carotid artery. The carotid artery begins with aortic arch and its bifurcated branches run through neck to head. The right carotid emerges from Brachiocephalic artery. The carotid bifurcation type structure leads to a complicated haemodynamic flow pattern. There are two carotid arteries in the human body, one in the left and another one at the right. The carotid artery is categorized into three segments, namely common carotid artery, internal carotid artery and external carotid artery. The presence of sinus-bulb at the internal carotid artery contributes to a stronger reversed flow [2]. The cerebral artery has also been studied thoroughly by many researchers [26, 27, 28], since it is susceptible to cerebral aneurysms. Haemodynamics of femoral artery [19, 20] needs attention, since its multiple bend structure is vulnerable to atherosclerosis. The femoral artery is one of the longest arteries in human body, which is situated in the thighs. Branches are very common geometrical features of arteries. In an artery, these branches may appear one after another emerging out of the mother artery as in celiac-superior mesenteric artery or opposite to each other with an offset distance, as in right-left renal arteries. Haemodynamical features in

the mother artery depends on the orientation and number of daughter branches [59]. Patient specific images of the aorta and the carotid artery can be seen in the Figure 2.2. The location of these arteries in the blood circulation network has been highlighted in the Figure 2.1.

(a) Aorta (b) Carotid artery

Figure 2.2: Aorta and Carotid artery.

2.3 Haemodynamical quantities

Haemodynamical quantities of prime importance are pressure, velocity, viscosity and shear stress. All these quantities are interrelated. The variation of one quantity with respect to other quantities can easily be determined using governing equations derived in the next chapter. These haemodynamical quantities play a significant role in judging the cardiovascular well being of humans. Any abnormal variation of these quantities in a diseased artery can lead to multiple organ failure.

2.3.1 Blood pressure

For a healthy adult, the typical systolic and diastolic values of pressure are 120 mmHg and 80 mmHg respectively. The blood pressure on vascular walls is higher for aged humans. This is due to decreased arterial yielding as a result of arteriosclerosis. For any human being irrespective of age and sex, blood pressure falls significantly during sleep. Other factors that contribute to the variation of blood pressure are static exercise, dynamic exercise, anger, sexual excitement and anxiety. Among all the arteries, the aorta experiences the highest blood pressure. The blood pressure can be measured *in vivo* with the aid of sphygmomanometer. In any artery, blood pressure can be computed *in silico* [24, 33]. *Maynard and Nithiarasu* [34] have computed pressure in an ascending aorta and other two locations in the arterial tree using locally conservative Galerkin (LCG) method. Blood pressure at any location in the body can be obtained by summing up pressure due to gravitational pull, heart force and frictional loss. In a vessel, if pressure at one point is known, pressure at another point can be calculated approximately using the relation [11].

$$p_1 - p_2 = \frac{1}{2}\rho v_2^2 - \frac{1}{2}\rho v_1^2 + \gamma h + \frac{\partial E}{\partial t} + \int_1^2 F_L \partial x \tag{2.1}$$

where p_1 and p_2 are pressures at two different points x_1 and x_2, ρ is density, v_1 and v_2 are velocities at two different points x_1 and x_2, γ is specific weight, h is height difference between two points x_1 and x_2, E is kinetic energy and F_L is frictional loss.

2.3.2 Role, nature and measurement of blood velocity

It is a well known fact that, higher the blood velocity higher will be the wall shear stress. This can be confirmed by the simulations presented in next chapters. The velocity of blood in an artery reaches its peak value during the systolic phase and will reach a negative value during the diastolic phase. Vascular blood velocity is always unsteady and pulsatile in nature. However, it is common to study steady flow in a specific region of an artery, in order to depict an average behavior of the flow [19, 1, 21]. It is not realistic to assume fully developed profile at the inlet. Since presence of bends and out of plane tortuosity prior to the inlet will make the flow profile asymmetric [16, 32]. However it is a common practice to assume fully developed flow at the inlet [24, 25] for idealized models. *In vivo* whole field blood velocity in any part of the body can be computed or monitored with higher resolution using various techniques such as laser doppler velocimetry, laser speckle contrast imaging, particle image velocimetry and nuclear magnetic resonance [35]. Unsteady velocity waveform at a cross section of an artery can be measured *in vivo* by the ultrasonic technique [30]. The generic Poisuelle parabolic profile is applicable to steady flows only. In idealistic models, the most widely used waveform is given by classical Womersley's solution [15, 36]:

$$u(x,t) = \frac{\hat{A}}{i\rho\omega}\left\{1 - \frac{J_0(i^{\frac{3}{2}}\alpha r/R)}{J_0(i^{\frac{3}{2}}\alpha)}\right\} e^{i\omega t} \tag{2.2}$$

where x and t are spatial and temporal dimensions respectively, $\hat{A}$ is a complex conjugate of pressure gradient [37], $i = \sqrt{-1}$, ρ is density of blood, ω is frequency of pulsatile flow, J_0 and J_1 are zeroth order and first order bessel functions respectively [15], R is vascular radius, r is the radius of a small element and $\alpha = R\sqrt{\frac{\omega}{\nu}}$ is Womersley number with ν as kinematic viscosity. The involvement of harmonics and other mentioned parameters make this profile more realistic. Typical Womersly spatial and temporal profiles calculated by the above equation are given in the Figure 2.3. This profile has been calculated for a patient specific carotid artery (Figure 2.2) by *Bevan et al* [80]. The harmonics and other parameters can be found in the same reference.

2.3.3 Viscosity of blood

Blood rheology is a vast field of study. This field is termed as haemorheology in clinical literature. Baskurt [40] has clearly linked peripheral vascular disease, hypertension and diabetes mellitus with abnormal haemorheology. Blood is viscoelastic and thixotropic under certain physiological conditions. Thurston [41] has proven the elastic nature of blood in unsteady flow conditions, experimentally and analytically. Blood also exhibits shear thinning behavior [38]. Blood is thinner when the shear forces that produce the flow are very high. Blood viscosity depends on plasma viscosity due to protein concentration and content of haematocrit [29].

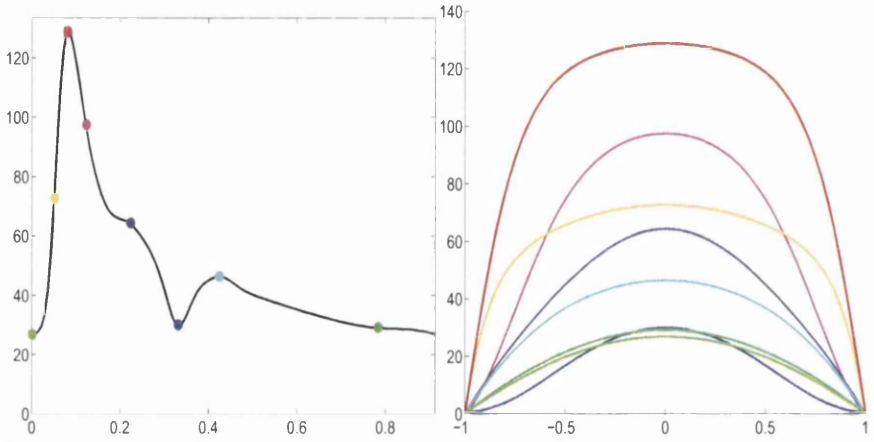

(a) Instants selected in temporal Womersley waveform (b) Spatial profile at selected instants

Figure 2.3: Womersly Profile.

Increased plasma viscosity due to haemodilution will decrease the wall shear stress drastically at a given shear rate. Blood viscosity also depends on shear strain rate of flow. Blood viscosity is inversely proportional to shear strain rate. Hardening of blood cells due to pathologies of aging, will increase viscosity [11]. In haemodynamical literature, varying viscosity is known as apparent viscosity. For vessels with diameter larger than 1 mm it is common to assume constant blood viscosity (i.e Newtonian flow) of about 0.035 Poise. Another factor that justifies the assumption of constant viscosity is shear strain rate. If shear strain rate of blood flow is higher than $100\ s^{-1}$, viscosity can be considered constant [47]. In this research work, a constant value of viscosity will be considered for all the problems, since the dimensions of vessels are greater than 1 mm. But, it is important to consider non-Newtonian behavior of blood in micro-vessels [43]. Blood viscosity μ in a vessel with radius R can be obtained by poiseuille's law:

$$\mu = \frac{-\Pi R^4}{8Q}\frac{\partial P}{\partial x} \tag{2.3}$$

where, Q is flow rate, $\partial P/\partial x$ is pressure gradient. Blood exhibits non-Newtonian behavior under various conditions. Blood is found to be non-Newtonian in the regions of flow separation and recirculation, and at low shear rates [59]. To model non-Newtonion behavior of blood in micro-vessels, there are various constitutive models available [48]. These include Casson model, Carreau-Yasuda model and K-L model.

2.3.4 Reynolds number

Reynolds number is a dimension-less number, which is the ratio of inertial forces to viscous forces. Reynolds number can reach as low as 1 in small arteries and veins [11]. A typical range of Reynolds of number in arterial flow is 0 to 5000. In the range 100 to 1000, inertial and viscous forces are equally influential. Due to this fact, vortical flow is always possible in arteries. Reynolds number is given by the equation:

$$R_e = \frac{u_{mean} D}{\nu} \tag{2.4}$$

Where, u_{mean} is mean velocity of blood flow, D is diameter of an artery and ν is kinematic viscosity of blood flow. From the above equation it is clear that, substantial decrease in hematocrit leads to turbulence, since viscosity of blood drops. In an arterial flow, Reynolds number can vary due to various physiological factors such as stenosis, curvature and presence of grafts [44]. In this research work, viscosity of blood is assumed to be constant. Therefore, velocity and dimensions are the only two factors responsible for variation of Reynolds number.

2.4 Structure of a blood vessel in brief

Blood vessels are one of the most intelligently built natural ducts. If all the blood vessels of a human are to be connected end to end, length is unimaginable. Like any other engineering cylindrical tube, blood vessels will also experience axial, hoop and radial stresses. The internal diameter of the vessel is known as lumen. The physiological zone of the vessel is categorized into three layers. These three layers are named as tunica intima, tunica media and tunica adventitia. For arteries, tunica intima is thick in nature. It consists of endothelium cells bonded by connective tissues. Endothelial is a single layer of endothelium cells present throughout the vascular system. It can be seen as an interface between blood and tissue. According to the experimental work by *Fry* [52], the yield stress for endothelium cells is about 380 dynes/cm^2. The stress beyond this value, due to haemodynamical pressure and wall shear stress can damage endothelium cells severely. The endothelial facilitates the transfer of nutrients from blood to tissues. The glycocalyx coating present in the endothelial is permeable to glucose, adrenalin and other nutrients and impermeable to plasma, since plasma is bigger in size. Thus plasma is retained in the blood. The central layer is known as tunica media, which is thin in nature. Internal elastic lamina separates the media from intima. The media consists of smooth muscle cells, which are combination of collagen and elastin. Smooth muscle cells are oriented circularly around the vessel. So that the contraction of these cells will decrease the lumen size. The outermost layer is known as tunica adventitia or tunica externa. External elastic lamina separates adventitia from media. In adventitia, fibroblasts and nerves are held together by collagen. Collagen is present in all three layers. The general vascular structure can be seen in the Figure 2.4 which has been reproduced from [81]. The structure of vessel remains same for veins. But the intima is thinner in veins.[45, 46]

2.5 Biological and physiological characteristics of blood in brief

Blood provides the required nutrients and oxygen to the tissue and takes away the carbon dioxide and waste products from the tissues. Thus, health of the tissues is greatly dependent on the characteristics of blood. The blood is also involved in the modulation of body temperature, acting defensive against infections and healing of injuries [39]. Elements of blood are white blood cells, red blood cells, platelets and plasma. Plasma, is the major constituent of blood. Content of plasma in the blood is more than 50 %. Thus, volume of plasma in the blood determines the viscosity of blood. Plasma is mainly water with a small portion of proteins. White

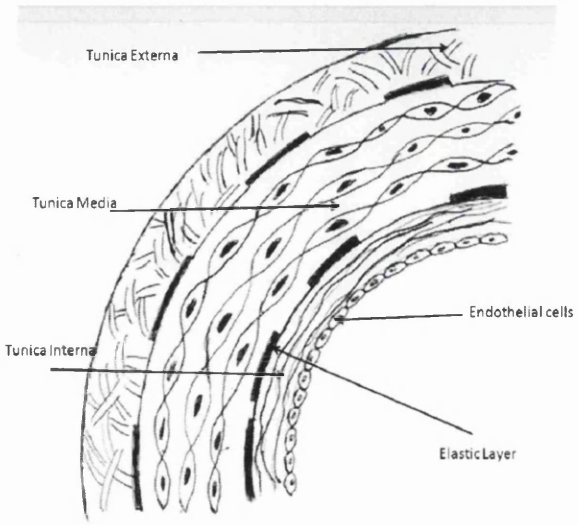

Figure 2.4: General vascular structure [81].

blood cells play a prominent role in immunity of human body. The white blood cells are also known as leukocytes are present in blood and lymph as well. Extremely larger or lower amount of leukocytes in the human body indicates a pathology. The red blood cells also known as erythrocytes are produced in the bone marrow. Erythrocytes are responsible for transportation of oxygen from lungs to tissues. Platelets are also known as thrombocytes. Thrombocytes are required to stop bleeding (haemostasis). Lower number of these cells can lead to excessive bleeding, whereas a higher number can lead to blood clots leading to thrombosis. The density of blood is about 1050 kg/m^3. On an average, a human body contains 4.5 to 6.0 L of blood [47].

Chapter 3

Flow features

3.1 Introduction to flow features

In the field of computational bio-fluid dynamics, qualitative numerical results are always presented in terms of flow features. These flow features include distribution of pressure and wall shear stress, velocity vectors and oscillatory shear index (OSI) in the case of unsteady flows. These flow features will be described briefly in the next sections. Flow features give a quick glance of physics in *in silico* biomedical models. Flow features facilitate easier identification of region of importance in the domain under study. The study of flow features and streamlines in order to understand the vascular blood flow dates back to 1945 [56]. In arteries, the region with abnormal and stronger flow patterns is more vulnerable for pathologies such as atherosclerotic plaque deposition and arterial dissection. Rupture of an aneurysm is always characterized by disturbed flow patterns [28]. Accuracy of *in silico* models can be determined by comparing numerically obtained flow features with those of experimental work. The flow features depend on the motion of fluid. In order to have a quick understanding of flow features, it is essential to know about the phase lag in the motion of fluid, due to inlet pressure. The flow in an artery can be divided into three regions, namely near wall, boundary layer and core [38]. Flow in the core region is dominated by inertia forces, thus phase lag is very low. Flow in the boundary layer involves balance between inertia and viscous forces, so the phase lag is moderate. Viscous dominant flow near wall experiences very significant phase lag. Pathologically, the importance of each hemodynamical quantity has been highlighted in the Table 3.1.

3.2 Haemodynamic pressure distribution

Pressure at every grid point is obtained by solving Naviers-Stokes equations. The pressure gradient or pressure drop depends on vascular diameter, flow rate, curvature or bifurcation angles if any, endothelial wall roughness and blood physical properties [38]. In any blood vessel, this pressure gradient is negative when the blood is accelerating and positive when the blood is decelerating with negative velocity [11]. For regular geometries such as a straight cylinder, pressure remains high at the inlet irrespective of the velocity. But for irregular geometries such as bends and bifurcation the peak pressure will shift to one of the bends or bifurcations at higher inlet velocities. For arteries with bends, the location of peak pressure depends on the angle and radius of curvature, and number of bends. For double bend arteries it is common to

locate peak pressure in the outer bend [24]. If the *in silico* model is symmetric, the pressure distribution in the symmetric plane (along the central axis) gives clear picture of pressure concentration in the whole model [19]. In case of arterial aneurysms, increase in peak pressure indicates the drastic growth of size and rupture [49]. *Ahmed et al* [50] have shown that, the pressure at peak systole, on an aneurysmal wall remains same as that of its parent artery, for an idealized cerebral aneurysm-model. *Papaharilaou et al* [16] have shown that, peak pressure in an idealistic abdominal aneurysm with an S-shaped inflow segment occurs near the distal end of sac. The pressure values at all the grid points become more significant, when arterial wall distensibility needs to be included in the numerical simulation. Since these pressure values are taken as boundary conditions for fluid structure interactions (FSI) simulations. The blood pressure distribution on the vascular wall of a typical thoracic aorta can be seen in the Figure 9.4 Chapter 9.

3.3 Velocity field

Velocity stream lines and associated contour plots are essential to understand the direction of flow and motion of fluid particles. In haemodynamical simulation, plotting of axial velocity profiles in symmetric plane is very common in bend and bifurcation type arteries [24, 19, 2, 25]. A strong asymmetric axial velocity profile at a cross-section indicates strong flow separation. In bend-arteries, axial velocity plots explain the intensity of centrifugal force on the bends. In bifurcation-type arteries, axial velocity plots determine the effect of bifurcation on flow in branches. In bend-type arteries, it is very important to visualize secondary flow. The secondary flow is given by velocity vectors parallel to the plane of cross section. The secondary flow is always characterized by recirculation zones at downstream. Secondary flow with recirculation can be seen in the Figure 6.5 of Chapter 6. Stronger secondary flow happens with increase in Reynolds number. This stronger secondary flow involves multiple vortices. The strength of secondary flow depends on intensity and angle of curvature, and number of bends. Under pulsatile conditions, *wood et al* have concluded in there work [20] that secondary flow in a femoral artery of male subjects is stronger than that of female subjects. The strength of secondary flow is given by Dean number D_e [38]

$$D_e = Re\sqrt{k_c} \tag{3.1}$$

where $k_c = \frac{R}{R_c}$, R being the radius of the artery and R_c being the radius of curvature. Higher the Dean number, stronger will be secondary flow. The Dean number is valid for laminar flows only. *Qiao et al* [24] have shown that secondary flow is stronger and complex for higher value of R. For femoral arteries, typical range of Dean number is 10-1000 [51, 20]. Complex secondary flow is characterized by multiple vortices. Apart from Dean number, the strength of secondary vortices also depend on the velocity profile at the inlet [32]. Multiple spiral vortices in the secondary flow are responsible for the accumulation of white blood cells such as macrophages and monocytes. The presence of these cells is believed to initiate and propagate lesions [75]. *Malinauskas et al* [76] have reported the elevated LDL (low density lipoprotein) permeability of the intima in a luminal location with complex secondary flow. Velocity vector plots also facilitate the identification of flow separation zones. Flow separation regions are very common in aneurysmal bulges and arterial sinus bulbs. Separation regions are responsible for the variation of shear and normal stresses on the arterial wall. A detachment point in a

separation region leads to low shear stress on walls. Whereas a reattachment point enforces relatively higher shear stress on the wall. If the reversed flow exists between the attachment and reattachment points, the arterial wall in this region is characterized by negative shear stress [53]. *O'Rourke et al* [17] have observed a detachment point followed by a strong recirculation zone in steady flow conditions and vortex shedding in systolic phase of pulsatile flow for a realistic abdominal aortic aneurysm. Flow separation is more pronounced [54] at the inflow region for balloon like expanding stents. *Nicholls et al* [55] have linked the flow separation zones in the bifurcation regions to atheroma. In multi-branched arteries, such as renal arteries, the occurrence of flow separation depends upon various parameters. These parameters include pulse rate, branch to trunk flow ratio and Reynolds number [57]. The presence of branches causes flow separation in mother artery. *Kim et al* [59] have observed flow separation regions in a location of mother artery, opposite to the renal branch. In this work, a high intensity flow separation has also been observed at branch locations proximal to the mother-branch junction. A stenosis in the aortic valve is responsible for flow separation region downstream in aorta. The occurrence and intensity of flow separation depends on the degree of the stenosis [58].

3.4 Wall shear stress distribution

Wall shear stress is the stress generated on the endothelial, due to shearing action of the blood particles on the wall. The shearing action is the result of tangential force component of the blood flow. The tangential force τ for a circular cross section can be calculated by classical poiseuille's equation:

$$\tau = \frac{4\mu Q}{\pi R^3} \tag{3.2}$$

where μ is viscosity of blood, Q is flow and R is radius of lumen. Experimental determination of the shear force involves measurement of wall shear rate with the aid of velocity profiles. These velocity profiles are usually obtained by techniques such as particle tracking, laser doppler, MRI and ultrasonic. In $in\ silico$ modeling of blood vessels, accurate computation of wall shear stress requires higher number of boundary layers near the wall. Numerically, wall shear stress τ_{wall} can be computed by the equation:

$$\tau_{wall} = (I - n \otimes n)\tau_{ij} \tag{3.3}$$

where, I is identity matrix, n is a normal vector, $\otimes$ will give the tensor product and τ_{ij} is Cauchy's stress. Two normals are used to remove normal stresses and retain tangential stresses. Cauchy's stress is given in the Equation 4.5 of Chapter 4. In numerical studies it is common to use wall shear stress as a parameter to perform grid convergence studies. In grid convergence studies, number of numerical models with different mesh densities will be solved. The model with desired accuracy of peak and average wall shear stress will be considered as the converged mesh.

Physiologically, abnormal variation of wall shear stress will distort the mechanical properties of endothelial layer. The experimental work done by *Fry* [52] proves that the wall shear stress beyond 380 dynes/cm^2 will distort endothelium cells. Any region of lumen exposed to low

wall shear stress is susceptible to atherosclerosis [60], since the blood moves slowly here. In the case of arteries with mild curvature multiple bends, high wall shear stress occurs in the intermediate region between two successive bends [19]. For high Reynolds number flow in the bend-type arteries, peak wall shear stress and peak pressure occur at a location near to each other. To confirm this, readers are referred to Figures 6.6 and 6.7. During the pulsatile flow in bend-type arteries, wall shear stress increases and decreases with velocity [24]. *Asakura and Karino* [3] have confirmed the presence of low wall shear stress and low fluid velocity in the internal radius of curvature of a coronary artery. This region is believed to be a favorable spot for atheroma. In bifurcation type arteries such as carotid, the wall shear stress largely depends on the angle between and dimensions of the internal and external carotid arteries. The arteries with bifurcations experience a sudden drop in wall shear stress at the start of bifurcation junction, due to increase in the cross sectional area [25] at the bifurcation. The carotid artery experiences peak wall shear stress at the apex of the bifurcation and very low wall shear stress at the external wall of the sinus bulb [5, 69]. Thus, the likelihood of plaque deposition in the sinus of a carotid is higher. *Yang et al* [66] have indicated the presence of WSS-maxima in the left carotid junction of aortic arch and peak WSS at right hand side of the aortic arch. Stress in an aneurysmal sac is usually low, but starting and end points of the sac are subjected to higher shear stresses [16]. According to the research done by *Shojima et al* [61], high wall shear stress initiates an aneurysm, low wall shear stress supports the growth of an aneurysm and wall shear stress at the tip of rupture of an aneurysm is found to be very low. Wall shear stress in an aneurysm largely depends on the angle of aneurysmal axis with respect to the plane of parent artery [67]. Accurate quantification of WSS in an aneurysmal wall requires the inclusion of wall elasticity [68]. For a precise understanding of the impact of wall shear stress on the endothelial, various indices have been developed. These indices are time averaged wall shear stress, wall shear stress gradients and oscillatory wall shear index. Wall shear stress gradient is $\partial\tau_w/\partial x$, where τ_w is WSS and x is the tangential wall coordinate. Other two indices are discussed in brief in the following two subsections. The WSS distribution on the vascular wall of a typical thoracic aorta can be seen in the Figure 9.5 of Chapter 9.

3.5 Oscillatory shear index

This index has been originally developed by *Ku et al* [62] in 1985, to study the abrupt variation of wall shear stress in a carotid bifurcation. It is given by:

$$OSI = \left[\frac{\left| \int_0^T \vec{\tau_w}^* \right| dt}{\left| \int_0^T \vec{\tau_w} \right| dt} \right] \tag{3.4}$$

Where T is time period and $\vec{\tau_w}^*$ is the stress component acting opposite to the temporal mean shear stress [62]. It is the most widely used index by the present generation of cardio-vascular research community, to determine the growth factor of haemodynamically triggered pathologies [24, 21, 28, 60]. The oscillatory shear index (OSI) captures the cyclic nature of wall shear stress on endothelial, due to the pulsatile blood flow. The definition of OSI is being changed by researchers over years, in order to make it more accurate. The latest definition of oscillatory shear index is given by [24, 63]:

$$OSI_{Latest} = \frac{1}{2}\left[1 - \frac{\left|\int_0^T \vec{\tau_w} dt\right|}{\int_0^T |\vec{\tau_w}| dt}\right] \tag{3.5}$$

In the above equation, OSI can vary between 0 and 0.5. Higher value of OSI indicates abrupt variation of wall shear stress. Higher OSI also implies stronger intensity of reversed flow. Reversed pressure gradient due to the high intensity retrograde inlet waveform in an artery causes the slow fluid near wall to reverse before the fluid in the center will reverse. This phase lag of flow will increase the OSI significantly [20]. Higher OSI contributes significantly to the pathogenesis of atherosclerosis [4]. In *in silico* simulation of carotid bifurcation, the OSI is sensitive to the outflow boundary conditions [64]. The apex and sharp sinus corner of the carotid bifurcation are more susceptible for higher OSI [65, 21]. Physical exercise will reduce the OSI significantly. *Lee et al* [63] have shown that, the regions of low and oscillatory shear stresses in an abdominal aorta found when the subject is resting, vanished under exercise conditions. The OSI distribution on the vascular wall of a typical thoracic aorta can be seen in the Figure 9.7 of Chapter 9.

3.6 Time averaged wall shear stress

The time averaged wall shear stress (TAWSS) is the mean of WSS values recorded at all the time steps. Like WSS gradient and OSI, time averaged wall shear stress can also be used as rupture index for aneurysms. Higher value of TAWSS contributes significantly towards the damage of endothelium. Time averaged WSS is given by:

$$\tau_{avg} = \frac{1}{T}\left[\left|\int_0^T \vec{\tau_w}\right| dt\right] \tag{3.6}$$

The distribution of TAWSS in an artery largely depends on the geometry [20]. Combination of low TAWSS and higher OSI is responsible for flow disturbances in arteries [64].

Table 3.1: Pathogenical importance of each blood flow feature.

Serial no	Hemodynamical quantities	Impact on vascular well being.
1	Abnormal hemodynamical Pressure	Responsible for growth after initiation and rupture of aneurysm
2	Abnormal axial flow	Responsible for flow separation and extrema of WSS
3	Abnormal secondary flow	Responsible for monocytes accumulation and increased particle residence time
4	Higher WSS	Responsible for endothelial cell damage
5	Lower WSS	Responsible for plaque accumulation
6	Abnormal WSSG	Responsible for endothelial cell damge
7	Abnormal OSI	Impact is similar to that of abnormal WSS (i.e. pathogenesis of atherosclerosis) for pulsatile flows
8	Abnormal TAWSS	Impact is similar to that of higher WSS (i.e. Damage to endothelial cells) for pulsatile flows

Chapter 4

Governing equations and solution scheme

4.1 Introduction

In physiological terms, science of blood flow and its impact in terms of forces and stresses on surrounding vascular wall is known as haemodynamics. Abnormal haemodynamics can cause harmful structural changes on endothelium and smooth muscle cells. These vascular changes in turn will cause haemodynamical anomalies. Strong eddy currents and flow separation are ideal examples for haemodynamical anomalies. The variation of physical quantities within the flow is necessary to understand the haemodynamic behavior. These typical physical quantities are velocity, pressure, density, temperature, normal stresses and shear stresses. There are various methods to determine these physical quantities. These methods include experimental, analytical and numerical. Performing experimental study to physically observe and measure physical quantities demands experimental setup and equipments. Analytical methods rely on theorems based on classical mechanics. But there are several limitations on analytical and experimental methods. On the other hand, we have numerical methods. In these methods, governing equations of fluid are solved numerically to obtain the values of physical quantities. This work involves extensive utilization of numerical methods to compute physical quantities. In the first section, governing equations of fluids are mentioned. The second section deals with the boundary conditions to be imposed on the governing equations of flow problems. The final part of this chapter presents an efficient numerical scheme dedicated to solve complex flow problems.

4.2 Governing equations of fluid dynamics

The whole science of fluid dynamics is based on three physical principles. They are conservation of mass, momentum and energy. For the purpose of computation, blood can be assumed as continuous. This assumption is based on the fact that the length scales are bigger than the mean free paths of blood cells in macro circulation. The behavior of such flows is dealt by a branch of mechanics known as continuum mechanics. In the context of continuum mechanics, flow of a fluid can be studied using any of the four flow models [10] namely, fixed control

volume, moving control volume, fixed infinitesimally small volume and moving infinitesimally small volume. Governing equations of fluid dynamics can be obtained by applying three physical principles to any one of the four flow models.

Continuity equation, considering a cartesian coordinate system can be obtained by applying the physical principle "mass is conserved" to a model of infitesimally small fluid volume fixed in space.

$$\frac{\partial \rho}{\partial t} + \nabla \cdot \rho V = 0 \tag{4.1}$$

where ρ is density (approximately 1050 kg/cm^3 for blood) , V is velocity vector and ∇ represents divergence.

Three momentum equations in conservative form, considering a cartesian coordinate system can be obtained by applying the physical principle "momentum is conserved" to a model of infitesimally small fluid volume fixed in space.

$$\frac{\partial \rho u}{\partial t} + \nabla \cdot V\rho u = -\frac{\partial p}{\partial x} + \frac{\partial \tau_{xx}}{\partial x} + \frac{\partial \tau_{xy}}{\partial y} + \frac{\partial \tau_{xz}}{\partial z} + \rho f_x \tag{4.2}$$

$$\frac{\partial \rho v}{\partial t} + \nabla \cdot V\rho v = -\frac{\partial p}{\partial y} + \frac{\partial \tau_{yx}}{\partial x} + \frac{\partial \tau_{yy}}{\partial y} + \frac{\partial \tau_{yz}}{\partial z} + \rho f_y \tag{4.3}$$

$$\frac{\partial \rho w}{\partial t} + \nabla \cdot V\rho w = -\frac{\partial p}{\partial z} + \frac{\partial \tau_{zx}}{\partial x} + \frac{\partial \tau_{zy}}{\partial y} + \frac{\partial \tau_{zz}}{\partial z} + \rho f_z \tag{4.4}$$

Where u, v and w are velocity components, p is pressure, τ_{ij} is a viscous stress tensor and f_i is force vector. The stress terms are functions of velocity gradients. These momentum equations are the result of Newton's second law ($Ma = F$). The right hand side of the momentum equations contains pressure gradient, viscous forces and body forces. It is important to note that the pressure gradient will turn positive, when the blood decelerates [11] due to pulsatile nature of flow.

The above quasi linear partial differential Equations 4.1 to 4.4 are the basic governing equations of fluid dynamics in conservative form. The governing equations can also be written in nonconservative form by assuming a model of moving infinitesimally small fluid volume. The governing equations in conservative form are suitable for incompressible flow problems, since they are easy to handle numerically in this case. The governing Equations 4.1 to Equations 4.4 all together are known as Navier-Stokes equations. The governing partial differential equations are nonlinear in nature and are difficult to solve analytically. To make the governing equations more suitable for a fluid like substance, the stress terms need to be replaced with velocity terms. This can be done by Cauchy's stress relation, in which deviatoric stress is given as

$$\tau_{ij} = \mu(\frac{\partial u_i}{\partial x_j} + \frac{\partial u_j}{\partial x_i} - \frac{2}{3}\delta_{ij}\frac{\partial u_k}{\partial x_k}) \tag{4.5}$$

Where μ is viscosity of blood, which fluctuates [8] due to factors such as diseases and body conditions (typical range is 0.03-0.05 poise) and δ_{ij} is Kroneckar delta. Kroneckar delta is unity if $i = j$ and is zero if $i \neq j$. For micro-vessels μ is plasma viscosity [60].

4.3 Boundary conditions

In a typical fluid dynamics problem involving an inlet and an outlet, boundary conditions are decided by characteristics. It is obvious that blood flow inside an artery is subsonic. If the subsonic flow is governed by hyperbolic type partial differential equations, there are two characteristics. For such a case, one boundary condition needs to be prescribed at the inlet and another one at the exit. In arterial haemodynamic simulations, it is common to prescribe a velocity profile at the inlet and pressure at the outlet. If dependent variables are defined at the boundary, the boundary conditions are Drichlet-type. On the other hand the boundary conditions are Neumann-type, if the derivatives of dependent variables are defined at the boundary. A mixture of both Drichlet-type and Neumann-type is also possible. This mixed type of boundary conditions is known as Robin type and is commonly found in convective heat transfer problems [12].

For a viscous flow, physical boundary conditions include no-slip condition, where all the velocity components are ignored at the wall (i.e. $u, v, w = 0$). No-slip condition means zero relative velocity between wall and immediate fluid. In arterial blood flow problems, no slip conditions are enforced on wall, since blood vessel wall distensibility is negligible. For idealistic arterial models a fully developed time dependent inlet velocity based on Womersley solution [15, 16] or *in vivo* measurements can be prescribed. It is a common practice to consider either zero pressure [17, 18] or setting second derivative of velocities and pressure in mean flow direction to zero at outlet [25]. In an artery, if the inlets and outlets are circular, velocity profile can be calculated using *Hagen-Poiseuille flow* equation:

$$u(x,t) = 2u_{mean}\left[1 - \frac{r(x)^2}{R^2}\right] \tag{4.6}$$

where u_{mean} is the mean velocity, $r(x)$ is the distance between a point x and the axis of the vessel and R is the radius of the blood vessel.

4.4 Generic form of governing equations

The governing equations 4.1 to 4.4 in conservative form can be represented generically by:

$$\frac{\partial V}{\partial t} + \frac{\partial F_i}{\partial x_i} + \frac{\partial G_i}{\partial x_i} = 0 \tag{4.7}$$

where,

$$V^T = (\rho, \rho u_1, \rho u_2, \rho u_3) \tag{4.8}$$

is the independent variable vector,

$$F_i^T = (\rho u_i, \rho u_i u_1 + \delta_{i1} p, \rho u_i u_2 + \delta_{i2} p, \rho u_i u_3 + \delta_{i3} p) \tag{4.9}$$

is the convective flux,

$$G_i^T = (0, -\tau_{i1}, -\tau_{i2}, -\tau_{i3}) \tag{4.10}$$

is the diffusive flux

4.5 Classical Numerical Schemes

To discretise a governing equation of fluids, there are numerous schemes available. These schemes include Stream line Upwinding Petrov Galerkin Schemes (SUPG), Taylor Galerkin Schemes and Charecteristic Galerkin Schemes. In the present work, the two methods, SUPG and TG schemes will be discussed for a typical 1D Convection Diffusion equation of a scalar variable given below.

$$\frac{\partial \psi}{\partial t} + u\frac{\partial \psi}{\partial x} - \nu\frac{\partial^2 \psi}{\partial x^2} = 0 \tag{4.11}$$

where ψ is a scalar variable.

4.5.1 Taylor Galerkin Approximation

In this scheme, Taylor expansion will be used for temporal discretisation and standard Galerkin approximation for spatial discretisation. For a typical Convection-Diffusion equation (Equation 4.11) given above, the solution scheme will yield:

$$\frac{\psi^{n+1} + \psi^n}{\Delta t} = \left[-u\frac{\partial \psi^n}{\partial x} + \nu\frac{\partial^2 \psi^n}{\partial x^2}\right] + \frac{\Delta t}{2}u^2\frac{\partial^2 \psi^n}{\partial x^2} + 0(\Delta t^2) \tag{4.12}$$

The above equation clarifies that the scheme gives second order accuracy in time. The added diffusion term $\frac{\Delta t}{2}u^2$ leads to a stable solution. After weakening the above equation using a standard galerkin weight, the resulting final matrix type equation is given below.

$$[M]\{\Delta\tilde{\psi}\} = \Delta t[[C]\{\tilde{\psi}\} + [D]\{\tilde{\psi}\} + [K]\{\tilde{\psi}\}]^n \tag{4.13}$$

Where, $\Delta\tilde{\psi} = \tilde{\psi}^{n+1} - \tilde{\psi}^n$, ˜represents nodal quantity, [M] is mass matrix, [C] is convection matrix, [D] is diffusion matrix and [K] is added diffusion matrix. For each element in the domain, the matrices are as given below:

$$[M] = \frac{l}{6}\begin{bmatrix} 2 & 1 \\ 1 & 2 \end{bmatrix}$$

$$[C] = \frac{u}{2}\begin{bmatrix} -1 & 1 \\ -1 & 1 \end{bmatrix}$$

$$[D] = \frac{\nu}{l}\begin{bmatrix} 1 & -1 \\ -1 & 1 \end{bmatrix}$$

$$[K] = -\frac{\Delta t u^2}{2l}\begin{bmatrix} 1 & -1 \\ -1 & 1 \end{bmatrix}$$

where l is length of an 1D element.

4.5.2 Stream line upwinding scheme

The importance of the SUPG lies in its weighting function. This weighting function will reduce the instabilities occurring perpendicular to the flow direction, since added diffusion acts only in the direction of flow. The SUPG weighting function is given below.

$$W^{*SUPG} = \frac{h}{2}\frac{\partial N^T}{\partial x}\frac{u}{|u|} \tag{4.14}$$

Where, h is element size, N is shape function and $|u|$ gives the magnitude of the velocity u. The term $\frac{u}{|u|}$ will determine the direction of streamline.

4.6 Non-Dimensional form of governing equations

To reduce the number of parameters and for programming convenience, all the governing equations can be non dimensionalized. The continuity equation can be written with indices,

$$\frac{\partial \rho}{\partial t} + \frac{\partial}{\partial x_i}(U_i) = 0 \tag{4.15}$$

Momentum equation can be written with indices,

$$\frac{\partial U_i}{\partial t} + \frac{\partial}{\partial x_j}(u_j U_i) = -\frac{\partial p}{\partial x_j} + \frac{\partial \tau_{ij}}{\partial x_j} \tag{4.16}$$

In the above equations $U_i = \rho u_i$ and the density term in the continuity equation can be replaced by:

$$\frac{\partial \rho}{\partial t} = \frac{1}{c^2}\frac{\partial p}{\partial t} \tag{4.17}$$

where c is the speed of sound. The above equation is valid for isentropic conditions only. Non dimensional form of governing equations can be obtained by using scales:

$$u^* = \frac{u_i}{u_\infty} : \rho^* = \frac{\rho}{\rho_\infty} : x_i^* = \frac{x_i}{L} : t^* = \frac{tu_\infty}{L} : p^* = \frac{p}{\rho_\infty u_\infty^2} \tag{4.18}$$

where, u_∞ is free stream velocity and ρ_∞ is free stream density and L is characteristic length. By using the above scales in Equations 4.15 and 4.16, non-dimensional continuity and moment equations can be written as:

$$\frac{\partial \rho^*}{\partial t^*} + \frac{\partial U_i^*}{\partial x_i^*} = 0 \tag{4.19}$$

$$\frac{\partial U_i^*}{\partial t^*} + \frac{\partial}{\partial x_j^*}(u_j^* U_i^*) = -\frac{\partial p^*}{\partial x_i^*} + \frac{1}{Re}\frac{\partial \tau_{ij}^*}{\partial x_j^*} \tag{4.20}$$

The deviotric stress Equation 4.5 can also be non-dimensionalized,

$$\tau_{ij}^* = (\frac{\partial u_i^*}{\partial x_j^*} + \frac{\partial u_j^*}{\partial x_i^*} - \frac{2}{3}\delta_{ij}\frac{\partial u_k^*}{\partial x_k^*}) \tag{4.21}$$

The non dimensional parameter Re is Reynolds number, given by $Re = \frac{u_\infty L}{\nu}$ and $\nu = \frac{\mu}{\rho_\infty}$ is kinematic viscosity.

4.7 Solution to the Navier Strokes equations using the characteristic-based split (CBS) scheme

This scheme is similar to the work done by *Chorin* [70] and can be applied to both compressible and incompressible flows. Whereas the Chorin's split was developed for incompressible Navier Strokes equations only. The CBS scheme is more stable due to the involvement of split and characteristic Galerkin. The scheme involves three steps. First step is determination of intermediate velocity using an intermediate momentum equation. Second step involves obtaining pressure by a continuity equation. In the third step, intermediate velocity is corrected to attain the final velocity. A fourth step can be included, if any scalar quantity such as temperature needs to be calculated. Initial temporal discretisation of the governing moment equation using Taylor series gives:

$$U_i^{n+1} - U_i^n = \Delta t\left[-\frac{\partial}{\partial x_j}(U_i u_j)^n - \frac{\partial p^{n+\theta_2}}{\partial x_i} + \frac{\partial \tau_{ij}^n}{\partial x_i}\right] + \frac{\Delta t^2}{2}u_k\frac{\partial}{\partial x_k}\left(\frac{\partial}{\partial x_j}(U_i u_j)^n + \frac{\partial p^n}{\partial x_i}\right) \tag{4.22}$$

The pressure term in the above equation will be calculated at a time $t^n + \theta\Delta t$. and $0 \leq \theta_2 \geq 1$.

$$\frac{\partial p^{n+\theta_2}}{\partial x_i} = \theta_2\frac{\partial p^{n+1}}{\partial x_i} + (1-\theta_2)\frac{\partial p^n}{\partial x_i} \tag{4.23}$$

Temporal discretization using three steps of CBS scheme are given below:

Step 1: Intermediate momentum

$$\Delta\tilde{U}_i = \tilde{U}_i - U_i^n = \Delta t \left[-\frac{\partial}{\partial x_j}(u_j Ui) + \frac{1}{Re}\frac{\partial \tau_{ij}}{\partial x_j} + \frac{\Delta t}{2} u_k \frac{\partial}{\partial x_k}\left(\frac{\partial}{\partial x_j}(u_j U_i)\right)\right]^n \tag{4.24}$$

where $U_i^n = U_i(t_n)$, $\Delta t = t^{n+1} - t^n$ and $\tilde{}$ indicates an intermediate quantity.

Step 2: Determination of pressure or density

$$\Delta\rho = \rho^{n+1} - \rho^n = \left(\frac{1}{c^2}\right)^n \Delta p = \left(\frac{1}{c^2}\right)^n (p^{n+1} - p^n) \tag{4.25}$$

$$= -\Delta t \left[\frac{\partial U_i^n}{\partial x_i} + \theta_1 \frac{\partial \Delta\tilde{U}_i}{\partial x_i} - \Delta t \theta_1 \left(\frac{\partial^2 p^n}{\partial x_i \partial x_i} + \theta_2 \frac{\partial^2 \Delta p}{\partial x_i \partial x_i} \right) \right] \tag{4.26}$$

Step 3: Momentum correction

$$\Delta U_i = U_i^{n+1} - U_i^n = \Delta\tilde{U}_i - \Delta t \frac{\partial p^{n+\theta_2}}{\partial x_i} \tag{4.27}$$

where $0.5 \leq \theta_1 \geq 1$. For explicit scheme $\theta_2 = 0$. An approximate integration backwards, gives these equations extra convection stabilization terms (last term in the RHS of step 1). These extra terms reduce oscillations due to highly convective flows. The above three steps coupled with energy equation and gas law forms a procedure to solve compressible flow problems. The spatial discretization of the governing equations using Galerkin method is given in the Section 4.9.

4.8 Artificial compressibility formulation

The compressible wave speed c in the step 2 is very large for incompressible fluid dynamic problems. For larger c, the solution scheme becomes stiff and impose severe time step restrictions. Therefore, the wave speed c should be replaced with an artificial parameter β. β is also known as artificial wave speed. The value of β chosen should be valid for any Reynolds number and any flow regime (diffusion and convection dominated). The values of β and Δt, which are found to be appropriate for accurate and faster solutions are given below:

$$\beta = max(\varepsilon, v_{\text{conv}}, v_{\text{diff}}) \tag{4.28}$$

where ε is a small constant (ε will not allow β to reach zero), v_{conv} is the convective velocity and v_{diff} is the diffusion velocity. These velocities can be calculated using the non-dimensional relations below:

$$v_{\text{conv}} = \sqrt{u_i u_i} \tag{4.29}$$

$$v_{\text{diff}} = \frac{2}{h_e Re} \tag{4.30}$$

where h_e is local element size and Re is the Reynolds number. The convection and diffusion coefficient are computed in a different manner for pre-conditioned AC schemes. But computing convection and diffusion coefficients by Equations 4.29 and 4.30 increases the performance of the scheme. The local element size at a node i in three dimensional (four noded tetrahedral elements) cases is given by:

$$h_i = min\,(3 \text{ volume/opposite face area})_{ie} \tag{4.31}$$

In the above equation, the minimum value is selected among the number of elements, ie, connected to node i. The local time step Δt is calculated as (in terms of non-dimensional quantities):

$$\Delta t = min(\Delta t_{\text{conv}}, \Delta t_{\text{diff}}) \tag{4.32}$$

where

$$\Delta t_{\text{conv}} = \frac{h}{v_{\text{conv}} + \beta} \tag{4.33}$$

and

$$\Delta t_{\text{diff}} = \frac{h^2 Re}{2} \tag{4.34}$$

In the equation 4.33, β is calculated from Equation 4.28. The calculated Δt is multiplied by a safety factor varying between 0.5 and 2.0 depending on the problem and mesh size. The best way to identify safety factor, is to start with maximum value and reduce until the scheme starts converging.

4.9 Spatial discretization and final matrices

The scheme employed in this work makes use of standard Galerkin method to descretize the governing equations in space. The general and intermediate velocity terms, and pressure term can be approximated as given below:

$$U_i = \mathbf{N_u}\overline{\mathbf{U_i}};\ \Delta U_i = \mathbf{N_u}\boldsymbol{\Delta}\overline{\mathbf{U_i}};\ \Delta \tilde{U}_i = \mathbf{N_u}\boldsymbol{\Delta}\overline{\tilde{\mathbf{U}}_\mathbf{i}} :\ p = \mathbf{N_p}\overline{\mathbf{p}} \tag{4.35}$$

where $\mathbf{N}$ are the shape functions and left hand side of all the terms represents nodal quantities. The above three steps of CBS-AC can be approximated using Galerkin method as below:

step 1: Weak form of intermediate momentum

$$\int_\Omega \mathbf{N_u^T}\Delta\tilde{U}_i\, d\Omega = \Delta t\left[-\int_\Omega \mathbf{N_u^T}\frac{\partial}{\partial x_j}(u_j U_i)d\Omega - \int_\Omega \frac{\partial \mathbf{N_u^T}}{\partial x_j}\tau_{ij}d\Omega\right]^n$$
$$-\frac{\Delta t^2}{2}\left[\int_\Omega \frac{\partial}{\partial x_j}(u_j\mathbf{N_u^T})\left(\frac{\partial}{\partial x_j}(u_j U_i)\right)d\Omega\right]^n + \Delta t\left[\int_T \mathbf{N_u^T}t_i^* n_i d\Gamma\right]^n \tag{4.36}$$

In the above equation t_i^* depicts the part of the deviatoric part of traction only and n_i are the outward normals to the boundaries. Weak form of pressure equation can be obtained by multiplying pressure term with standard Galerkin weight and replacing c with AC parameter β as given below.

Step 2: Weak form of pressure equation

$$\begin{aligned}\int_\Omega \mathbf{N_p^T}\left(\frac{1}{\beta^2}\right)^n \Delta p \, d\Omega &= -\Delta t \int_\Omega \mathbf{N_p^T}\frac{\partial}{\partial x_i}\left(U_i^n + \theta_1 \Delta \tilde{U}_1 - \theta_1 \Delta t \frac{\partial p^{n+\theta_2}}{\partial x_i}\right) d\Omega \\ &= -\Delta t \int_\Omega \mathbf{N_p^T}\frac{\partial}{\partial x_i} U_i^n d\Omega + \Delta t \theta_1 \int_\Omega \frac{\partial \mathbf{N_p^T}}{\partial x_i}\left(\Delta \tilde{U}_i - \Delta t \frac{\partial p^{n+\theta_2}}{\partial x_i}\right) d\Omega \\ &\quad -\Delta t \theta_1 \int_\Gamma \mathbf{N_p^T}\left(\Delta \tilde{U}_i - \Delta t \frac{\partial p^{n+\theta_2}}{\partial x_i}\right) n_i d\Gamma \end{aligned} \tag{4.37}$$

Step 3: Weak form of momentum correction

$$\int_\Omega \mathbf{N_u^T}\Delta U_i d\Omega = \int_\Omega \mathbf{N_u^T}\Delta \tilde{U}_i \, d\Omega - \Delta t \left[\int_\Omega \frac{\partial \mathbf{N_u^T}}{\partial x_i}((1-\theta_2)p^n + \theta_2 p^{n+1}) d\Omega\right] + \int_\Gamma \mathbf{N_u^T} t_i^{**} n_i d\Gamma \tag{4.38}$$

The missing traction part of pressure in the step 1 can be found in the above equation as t_i^{**}. The finite element discretiztion facilitates the enforcement of traction boundary conditions, naturally. The CBS-AC scheme is advantageous for traction prescribed problems, since it is not essential to explicitly prescribe Drichlet conditions for pressure in this scheme. The final matrix of the discretized governing equations are obtained by including Equations 4.35 in the Equations (4.36)-(4.38).

Step 1: Intermediate momentum

$$\Delta \overline{\tilde{U}} = -\mathbf{M}_u^{-1}\Delta t[(\mathbf{C}_u \overline{\mathbf{U}} + \mathbf{K}_\tau \bar{\mathbf{u}} - \mathrm{f}) - \Delta t(\mathbf{K}_u \overline{\mathbf{U}})]^n \tag{4.39}$$

Step 2: Pressure

$$(\tilde{\mathbf{M}} + \Delta t^2 \theta_1 \theta_2 \mathbf{H})\Delta \overline{\mathbf{p}} = \Delta t[-\mathbf{G}\overline{\mathbf{U}}^n + \theta_1 \mathbf{G}\Delta \overline{\tilde{\mathbf{U}}} - \Delta t \theta_1 \mathbf{H}\overline{\mathbf{p}} - \mathbf{f_p}]^n \tag{4.40}$$

Step 3: Momentum correction

$$\Delta \overline{\mathbf{U}} = \Delta \overline{\tilde{\mathbf{U}}} - \mathbf{M_u}^{-1}\Delta t[\mathbf{G}^T(\overline{\mathbf{p}}^{\mathbf{n}} + \theta_2 \Delta \overline{\mathbf{p}})] \tag{4.41}$$

where

$$\mathbf{M}_u = \int_\Omega \mathbf{N_u}^T \mathbf{N_u} d\Omega; \quad \mathbf{K}_\tau = \int_\Omega \mathbf{B}^T \mu \left(\mathbf{I}_0 - \frac{2}{3} \mathbf{m}\mathbf{m}^T \right) \mathbf{B} \; d\Omega; \quad \mathbf{f} = \int_{\Gamma_t} \mathbf{N_u}^T \mathbf{t}^* d\Gamma$$

$$\mathbf{H} = \int_\Omega (\nabla \mathbf{N_p})^T \nabla \mathbf{N_p} d\Omega; \quad \tilde{\mathbf{M}} = \int_\Omega \mathbf{N_p}^T \left(\frac{1}{\beta^2} \right)^n \mathbf{N_p} d\Omega; \quad \mathbf{G} = \int_\Omega (\nabla \mathbf{N_P})^T \mathbf{N_u} d\Omega$$

$$\mathbf{f_p} = \Delta t \theta_1 \int_\Gamma \mathbf{N_p}^T (\Delta \mathbf{U}^* - \Delta t \nabla p^n) \mathbf{n}^T d\Gamma; \; \mathbf{K_u} = -\frac{1}{2} \int_\Omega (\nabla^T (\mathbf{u N_u}))^T (\nabla^T (\mathbf{u N_u}) d\Omega \quad (4.42)$$

where $\mathbf{B} = \mathbf{S}\mathbf{N_u}$, $\mathbf{S}$ is an appropriate strain matrix or operator obtained from deviatoric stress Equation 4.21 and $\mathbf{N_u}$ is the shape function. In 3D space $\mathbf{m} = [1, 1, 1, 0, 0, 0]^T$ and

$$I_0 = \begin{bmatrix} 2 & & & & & \\ & 2 & & & & \\ & & 2 & & & \\ & & & 1 & & \\ & & & & 1 & \\ & & & & & 1 \end{bmatrix}$$

Chapter 5

Flow through a straight artery with constant circular cross section

5.1 Introduction

A straight artery/tube with constant radius 0.3 cm and length 8 cm has been studied for various Reynolds numbers. Steady flow simulation of an artery at various Reynolds numbers gives an averaged [22] behavior of pulsatile flow simulation. The typical range of radius based on lumen diameter is 0.3 cm to 0.9 cm [19, 24, 21, 1, 29] for idealistic arterial models. This study will represent a straight section of a healthy artery. It is not expected to observe any abnormal flow patterns in this straight artery, since the flow remains developed (poiseuille's) throughout the length. But complete understanding of flow behavior in a straight artery is essential, since it forms the benchmark for a study of arteries diseased with stenosis and aneurysms. For a straight tube, analytical solutions for pressure drop and wall shear stress are available. Because of this reason, a numerical solution on the straight artery/tube has been performed, in order to validate the numerical scheme. The numerical predictions of WSS and pressure are found to be in good agreement with analytical (poiseuille's) calculations.

5.2 Numerical model and boundary conditions

In order to calculate accurate values of wall shear stress, the geometrical domain has been discretized with boundary layers. An in house mesh generator known as FLITE3D has been used to discretize the domain. The finite element grid with boundary layers consisted 220454 tetra elements and 62503 nodes. Average element size in the model is 0.03 cm and number of boundary layers is eight. The mesh is of uniform longitudinal spacing and thickness of the edge boundary layer is 0.002 cm. The total boundary layer thickness is 0.077 cm. Figure 5.1 shows the mesh with boundary layers. The boundary conditions include no slip condition at the wall and fully developed velocity profile at the inlet. The assumptions made in the numerical simulation are similar to those made by many authors [19, 24]. These include rigid arterial wall, incompressible, Newtonian, steady and laminar flow. The governing Navier Stokes

equations of blood flow have been solved with the aid of the explicit-artificial compressibility scheme based on CBS method [14]. The solution methodology has already been presented in the previous chapter. The steady blood flow simulation has been carried out for 5 cases with varying Reynolds numbers (120, 240, 480, 960 and 1920). These Reynolds numbers are chosen based on cardiac cycle, Re-1920 being peak systolic flow. The Reynolds number is calculated, by considering the maximum inlet velocity and vascular diameter. In order to overcome the pressure oscillation difficulties, safety factor used is 0.5. The pseudo iterations were performed until the L2-norm of velocity and pressure errors reached 10^{-5}.

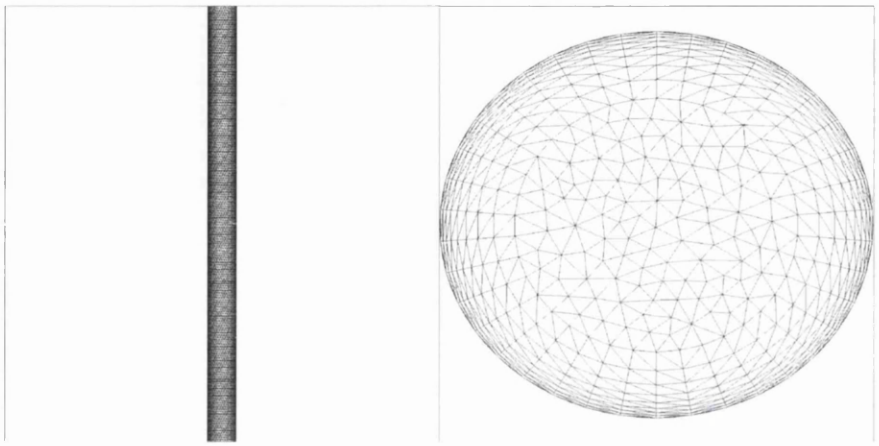

(a) Surface mesh (b) Cross-sectional view of the mesh

Figure 5.1: Mesh and boundary layers for a straight artery with constant radius.

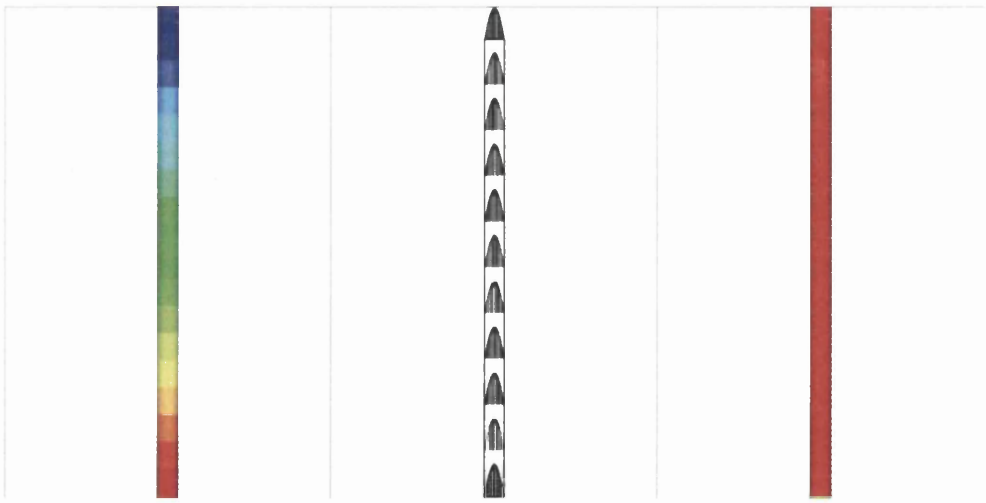

(a) Pressure distribution (b) Axial velocity vector plot (c) Wall shear stress distribution

Figure 5.2: Flow through a straight artery at Re-120.

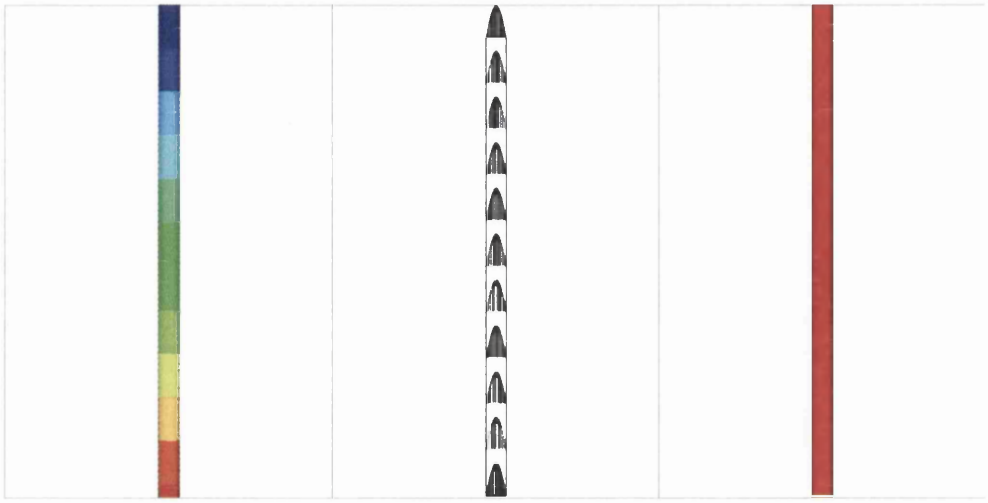

(a) Pressure (b) Velocity vector (c) Wall shear stress

Figure 5.3: Flow through a straight artery at Re-1920.

Table 5.1: A straight artery: Results (in dynes/cm^2) for five different Reynolds numbers.

Re	Max pressure	Δp	Peak WSS	Poisuelle's Δp	Poisuelle's WSS
120	113.3	113.3	2.015	108.08	2.02
240	227.2	227.2	4.025	216.17	4.053
480	459.6	459.61	8.125	432.34	8.10
960	914.5	914.5	16.825	864.68	16.21
920	1802.2	1802.2	32.42	1729.36	33.0

5.3 Results and discussions

Figures 5.2 and 5.3 show pressure, velocity vector and WSS plots for the Reynolds numbers 120 and 1920 respectively. From these two figures, it can be noted that maximum axial velocity remains at the center for all the sections and both the cases. Same trend has also been found for Reynolds numbers 240, 480 and 960 (Figures not shown here). This is due to the fact that there is no variation in cross section and the tube is straight. In this straight artery, the primary (axial) flow dominates throughout the length and no secondary flow occurs at any cross section. By observing the Figures 5.2c and 5.3c, we can conclude that the wall shear stress remains constant along length, since velocity gradient remains same at all the cross sections. Pressure contour plots suggest a pressure drop in all the cases, which is due to frictional losses. Table 5.1 gives the values of maximum pressure, pressure drop, poiseuille's pressure drop, wall shear stress and poiseuille's WSS at five Reynolds numbers (i.e. 120, 240, 420, 960 and 1920). Pressure and wall shear stress values are in dynes/cm^2. Pressure drop remains same as maximum pressure, since exit pressure is zero. From this table, it is evident that the pressure drop increases with the Reynolds number. Table also proves that the peak wall shear stress increases with Reynolds number, due to the increasing flow rate. Since the lumen is completely cylindrical and the flow is fully developed, Hagen Poiseuille equation can be employed to calculate pressure and wall shear stress, analytically. The Table

5.1 contains calculated pressure drop for five Reynolds numbers using the Hagen Poiseuille equation ($\Delta P = 8\mu u_{avg} l Q/\pi r^4$), where l is length of straight cylinder in cm, u_{avg} is average axial velocity in cm/s, r is the radius of straight artery in cm and Q is the flow rate in cm^3/s. The analytical values of wall shear stress for five Reynolds numbers using Hagen Poiseuille equation ($\tau_{wall} = 4\mu Q/\pi r^3$) is given in the last column of the Table 5.1. The analytical pressure drop and wall shear stress values are found to be in good agreement with those calculated numerically. For wall shear stress, the error due to numerical discretion is less than 0.2 % for all the Reynolds numbers. The pressure drop calculated numerically, is also in good agreement with analytical solution, since error due to numerical discretization is below 5 % for all the Reynolds numbers. This numerical-analytical correlation justifies the convergence of mesh. Because of this supporting fact, the same average element size (i.e. 0.03 cm) and same number of boundary layers have been used for spatial dicretization of all the idealistic artery-models in the forthcoming chapters. The numerical solution has also been attempted for four other models (4, 5, 6 and 7 boundary layers). The edge thicknesses for each model are give in Table 5.4. But the mesh with 8 boundary layers has given numerical WSS value, which are very close to the analytical values. This can be confirmed by referring to Figure 5.4 and Table 5.2.

Table 5.2: A straight artery: WSS convergence for 5 different Boundary Layers.

Number of BLs	Edge size	WSS
4	0.005	31.2
5	0.004	31.54
6	0.0036	31.92
7	0.0031	32.3
8	0.002	32.42

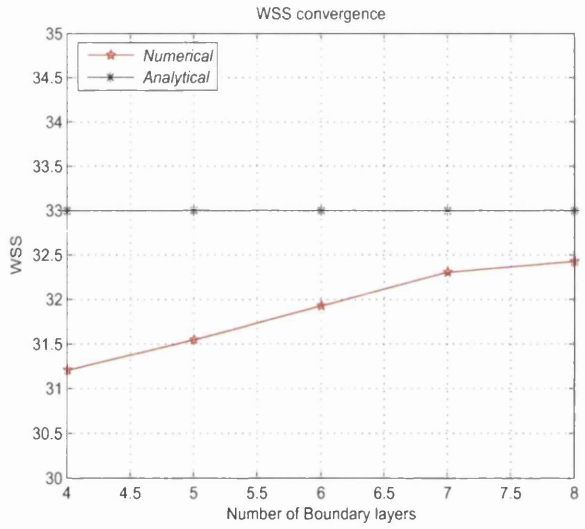

Figure 5.4: A straight artery: WSS for 6 models with different Boundary Layers.

Chapter 6

Flow through a model artery with a 90 degree bend

6.1 Introduction

A curved tube with constant diameter (D = 0.6 cm), inlet section length 5D, 90 degree bend with a radius of curvature 2.8D and an outlet section length 3D has been studied for various Reynolds numbers. In order to validate the solution, the geometrical features chosen here are based on the research work conducted by *Rabiee et al* [31]. This study will represent a curved section of a healthy artery. This type of bend structure is a possibility in almost all the arteries in the human body. Complete understanding of flow behavior in a curved artery is essential, since it forms the benchmark for a study of an artery with bends. Hemodynamical studies of curved arteries is highly essential in the field of biomechanics, since the presence of curvature will induce centrifugal forces on the walls. The flow patterns, pressure gradient and wall shear stresses vary significantly as a consequence of this centrifugal force. The centrifugal force in the curved artery is also responsible for the formation of complex secondary flow (vortices) downstream. However, the strength of the secondary flow largely depends on the intensity of the centrifugal force. Physiologically, all of these centrifugally induced abrupt flow features will induce pathologies such as hyperplasia, atherosclerosis and arterial dissection.

6.2 Numerical model and boundary conditions

The finite element grid with boundary layers consisted of 269032 elements. Average element size in the model is 0.03 cm and number of boundary layers is eight. The mesh is of uniform longitudinal spacing and thickness of the edge boundary layer is 0.002 cm. The total boundary layer thickness is 0.077 cm. The mesh generation algorithm and the CFD solver used are same as those in previous chapter. Figure 6.1 shows the mesh and boundary layers. The boundary conditions prescribed are no slip condition at walls and fully developed flow at the inlet. The assumptions made in the numerical simulation are similar to those made in previous problem. These include rigid arterial wall, incompressible, Newtonian, steady and laminar flow. The steady blood flow simulation has been carried out for five different Reynolds numbers (i.e. 120, 240, 480, 960 and 1920). The pseudo iterations were performed until the L2-norm of

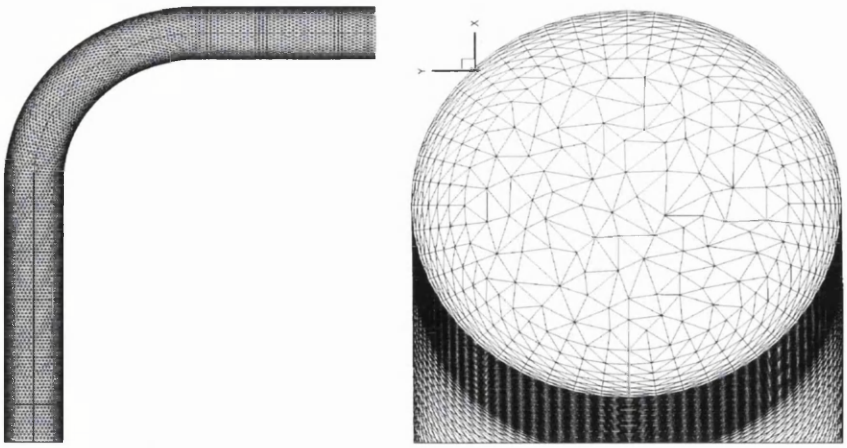

(a) Surface mesh (b) Cross-sectional view of the mesh

Figure 6.1: Mesh for an artery with single bend.

velocity and pressure errors reached 10^{-5}.

6.3 Results and discussions

1. Figure 6.2 depict axial velocity of flow in the symmetric plane for five Reynolds numbers.

2. The flow along the length is termed as primary flow, whereas the flow along the plane perpendicular to the length of artery is termed as secondary flow. The same terminology has been used throughout the thesis.

3. Three sections have been selected for qualitative studies of secondary flow. The numbering of the sections start from the section proximal to the inlet, third one being the section proximal to the outlet. The three sections are shown in Figure 6.3. Figures 6.4 and 6.5 represent secondary flow for Reynolds numbers 120 and 1920. Left hand side of the circles is towards inner curvature of the bend.

4. The wall shear stress contour plots for the single bend artery at two different Reynolds numbers, are given in Figure 6.6.

5. The pressure distribution for the single bend artery at various Reynolds numbers has been shown in Figure 6.7.

6. For the pressure and WSS contour, scale chosen to each plot is different. This has been done to capture the spatial variation of WSS and pressure.

7. In order to understand the spatial variation of WSS on vascular wall, peak WSS on each of the three geometrical sections has been tabulated in the Table 6.2. The three sections are inlet straight section, bend and outlet straight section.

Table 6.1: An artery with single bend: Results (dynes/cm^2) for five different Reynolds numbers.

Re	Maxpressure	Pressuredrop	Peak WSS
120	91.8	91.8	2.95
240	199.0	199.0	7.6
480	448.0	448.0	20.25
960	1007.6	1007.6	52.25
1920	3148.18	3148.18	123.6

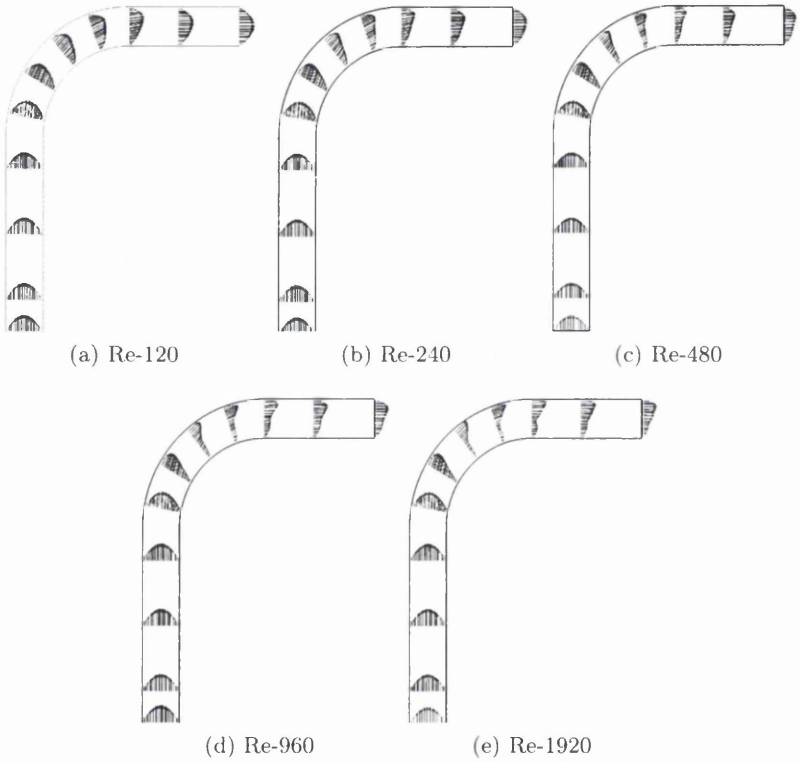

(a) Re-120 (b) Re-240 (c) Re-480

(d) Re-960 (e) Re-1920

Figure 6.2: An artery with single bend: Axial velocity profiles (X-Z plane).

6.3.1 Velocity profile in symmetric plane

Effect of centrifugal force on velocity profile at the bend is evident from the Figure 6.2. At lower Reynolds numbers (i.e. 120), the velocity profile at the exit is fairly uniform. But at higher Reynolds numbers, the maximum of axial velocity shifts outwards. This phenomenon has already been observed by *Hoogstraten et al* [19]. The axial velocity flow pattern obtained here is similar to those obtained by *Rabiee et al* [31]. At higher Reynolds numbers, as the flow enters the bend, the developed flow deviates and the peak of primary flow velocity shifts to external curvature, since fluid particles are centrifugally pushed towards the outer wall. Because of this peak velocity shifting-effect, the vascular wall region of the external curvature is subjected to higher WSS (Figure 6.6). The double peak axial velocity, which can be seen

proximal to the end of bend is responsible for the formation of double vortex secondary flow [77].

6.3.2 Secondary flow in cross sections

From the previous chapter it is clear that the complex secondary flow is not expected in a straight tube. Based upon this fact, no sections have been selected in straight inlet section. Three sections have been chosen in the bend region (Figure 6.3) including the one at the end of bend region. In the section-b (Figure 6.3), the peak value of secondary flow velocity is found to be 25 % of that of primary flow velocity. Whereas in a section distal to the bend, the peak value of secondary flow velocity is found to be 5 % of that of primary flow velocity. This indicates that primary flow dominates over secondary flow, once the flow reaches the end of straight outlet. The strong secondary flow in terms of vortices can be observed at the end of bend only (Figures 6.4 and 6.5). This supports the fact that, in vascular bends strong secondary flow appears downstream [24]. At higher Reynolds numbers, secondary flow down stream becomes more complex due to increase in the number of vortices. Approaching turbulence due to higher Reynolds number is responsible for this complex secondary flow. Additionally, we can confirm that secondary flow at all the Reynolds numbers, is always directed towards inner curvature. The same effect has also been observed at a location of straight inlet section proximal to the bend. This effect can be termed as early bend effect. Whereas the strong secondary flow appearing distal to the bend can be termed as late bend effect. The early bend effect is a consequence of flow impingement and the inertia. Where as the late bend effect is due to the interaction between early bend effect and the centrifugal force. The early bend effect pushes the fluid towards internal curvature. The centrifugal force pushes back the fast moving fluid at the center of the artery towards the external curvature. This combination of centrifugal force and early bend effect creates a multiple vortex secondary flow pattern. This pattern can be observed downstream only, since the strength of centrifugal force is higher at the end of bend. This occurrence of higher centrifugal force at the end of bend can be clarified by velocity profiles given in the Figure 6.2. At higher Reynolds number, the secondary flow distal to the bend appears as a horse shoe vortex (Figure 6.2). The luminal regions involving secondary vortices are associated with subendothelial macrophage accumulation [75]. The increased accumulation of macrophage in a plaque inflicted artery initiates and propagates lesion.

6.3.3 Wall shear stress contour plots

The Table 6.1 indicates that the peak wall shear stress increases with Reynolds number. The value of peak wall shear stress doubles when the Reynolds number is increased by two times. According to the Figure 6.6, at lower Reynolds number (120), wall shear stress concentration appears after the end of the bend. Since the strength of the centrifugal load is not enough to produce strong impingement of fluid particles on the external curvature wall of the bend and slower fluid particles will directly shear on the wall at the end of bend. But at higher Reynolds numbers (Figure 6.6 Re-1920) the peak wall shear stress is concentrated on the outer curvature of the bend. Since stronger centrifugal force impinges and shears fast moving moving fluid particles on the external curvature of the wall. Also, a small WSS concentration can be observed at the internal curvature of the beginning of the bend (view not shown here). This WSS concentration is purely due to the early bend effect. This will disappear at higher

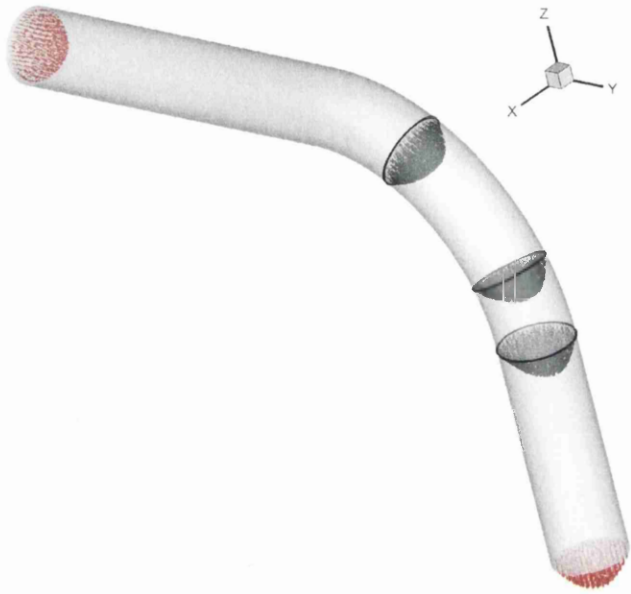

Figure 6.3: An artery with single bend: Three sections chosen for secondary flow.

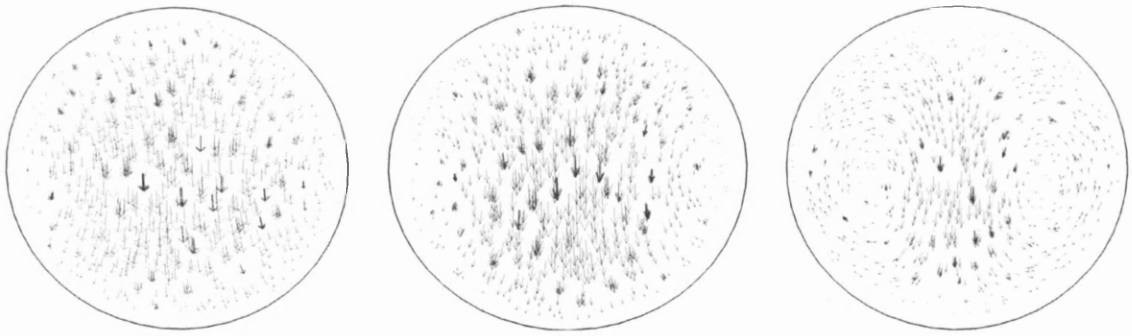

(a) Section a (b) Section b (c) Section c

Figure 6.4: An artery with single bend: Secondary flow (X-Y plane) in three cross sections at Re-120.

Reynolds numbers. At a given Reynolds number, the WSS value is found to be higher than that of the straight section in the previous chapter. This indicates that presence of curvature increases the peak WSS. According to the Table 6.2, the WSS value in the straight inlet region is very close to that of Poiseuille flow, calculated in the previous chapter. As compared to the straight artery in the previous chapter, a slight difference in WSS happens in the straight inlet of this artery, due to early bend effect. The bend region is subjected to higher WSS, due to the flow impingement on the wall of external curvature. This impingement of the particles is a consequence of peak axial velocity at the external curvature of the bend. At higher Reynolds numbers, the WSS value in the straight outlet is closer to that of the bend. At lower Reynolds number, the straight outlet tries to regain the WSS value of a Poiseuille flow.

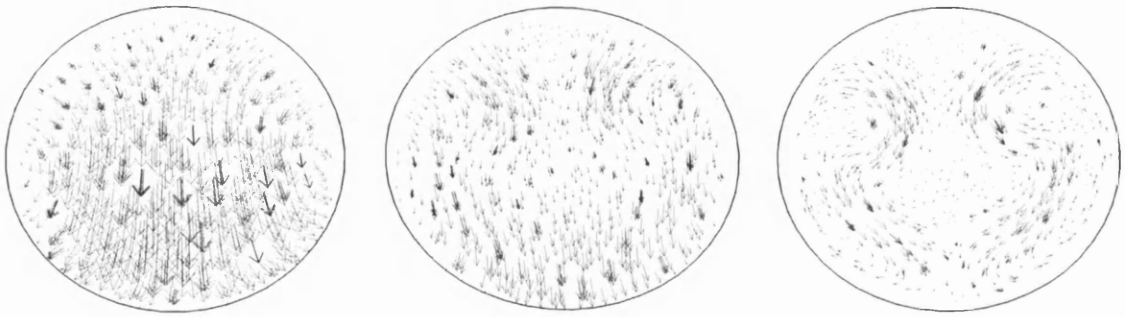

(a) Section a (b) Section b (c) Section c

Figure 6.5: An artery with single bend: Secondary flow (X-Y plane) in three cross sections at Re-1920.

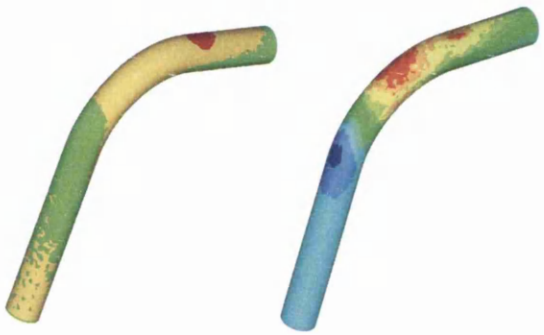

(a) Re-120 (b) Re-1920

Figure 6.6: An artery with single bend: wall shear stress (Peak values are given in Table 6.1).

Table 6.2: An artery with single bend: Peak wall shear stress (dynes/cm^2) in three entities.

Re	Inlet	Bend	Outlet
120	2.64	2.95	2.145
240	4.96	7.6	4.865
480	9.16	20.25	12.2
960	19.01	52.25	46.8
1920	33.3	123.6	115.69

6.3.4 Pressure distribution

The variation of pressure with respect to Reynolds number has been given in Table 6.1. The pressure drop is same as maximum pressure, since the exit pressure is zero. Higher pressure drop at higher Reynolds numbers can be noticed from the table. By observing the pressure distribution given in Figures 6.7, we can conclude that at lower Reynolds numbers, qualitative pressure distribution is roughly same as that of a straight tube in the previous chapter. But at higher Reynolds numbers, highest pressure can be observed at the outer curvature of the bend. This effect indicates the presence of stronger centrifugal force at higher Reynolds numbers.

(a) Re-120 (b) Re-240 (c) Re-480

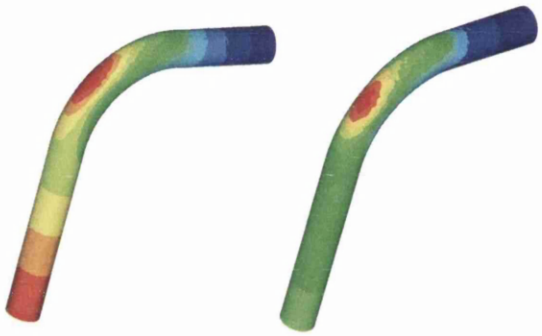

(d) Re-960 (e) Re-1920

Figure 6.7: An artery with single bend: Pressure distribution at five different Reynolds numbers (Peak values are given in Table 6.1).

The centrifugal force F_c is given by

$$F_c = \frac{mv^2}{r} \tag{6.1}$$

Where m is mass, v is velocity of fluid and r is radius of curvature of bend. The equation indicates that the higher velocity at outer curvature of the bend amplifies the centrifugal force on the wall. At higher Reynolds numbers, the pressure drop is found to be higher than that of the straight section in the previous chapter. This proves that presence of curvature leads to higher pressure drop. We can also conclude that the presence of curvature leads to impingement of the fluid particles on the outer wall of the curved segment, resulting in higher pressure on this region. This centrifugal force-impingement driven pressure has been observed at higher Reynolds numbers only.

Chapter 7

Flow in a model artery with two bends of 35 degree each

7.1 Introduction

A double curved tube with constant radius (D= 0.6 cm), inlet section length 1.5D, two 35 degree bends with a radius of curvature 7.5D and an outlet section length 2.5D has been studied for various Reynolds numbers. In order to validate the solution, the geometrical features chosen here are based on the research work conducted by *Hoogstraten et al* [19]. In this chapter, the steady state solution for the double curvature artery has been presented for various Reynolds number flows. The Reynolds numbers selected are 120, 240, 480, 960 and 1920. The Reynolds numbers above 1000 usually corresponds to exercise conditions. Whereas below 1000 corresponds to resting conditions [22]. This study will represent flow through the curved sections of femoral artery, since curvatures present in this idealized artery resemble with those of femoral artery [20]. This study involves two bends. However, the curvature and number of successive bends in a femoral artery depends on the subject's posture. Both the bends are in same plane of symmetry and, planes of inlet and outlet are parallel to each other. Such geometrical features are common in femoral arteries [77]. Arteries with multiple curvatures are of physiological importance, since these curvatures will introduce aberrant flow patterns and abrupt variation of wall shear stress. The curvature induced abnormal wall shear stress and blood pressure are expected to be leading cause of atherogenesis. Whereas curvature induced complex secondary flow is believed to be responsible for accumulation of monocytes and macrophages on the endothelium [75]. This analysis is based on the research done by *Hoogstraten et al* [19]. The main objective of this chapter is to explore the qualitative and quantitative primary/axial flow , secondary flow patterns, wall shear stress and pressure in an artery with two mild curvature-bends. In order to understand the flow behavior in various sections of the artery, the spatial domain can be divided in to four entities. These entities are straight outlet, first bend, second reverse-bend and straight outlet. We will discuss about the flow patterns in all these entities. The value of WSS in the straight inlet is found be in good agreement with analytical solution (Poiseuille flow). This agreement serves as a validation of mesh and the CFD code.

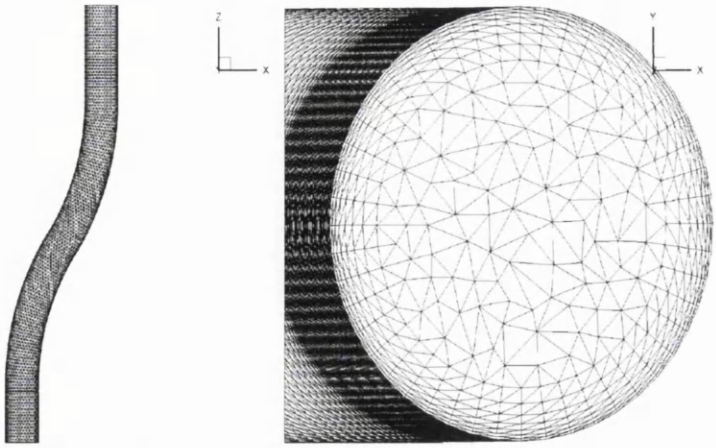

(a) Surface mesh in X-Z Plane (b) Cross-sectional view of the mesh

Figure 7.1: An artery with two mild curvatures: Meshed model.

7.2 Numerical model and boundary conditions

The finite element grid with boundary layers consisted 322137 elements and 56674 nodes. Average element size in the model is 0.03 cm and number of boundary layers is eight. This element size has given a converged solution in the straight artery (refer Chapter 5). The mesh is of uniform longitudinal spacing and thickness of the edge boundary layer is 0.002 cm. The total boundary layer thickness is 0.077 cm. The mesh generation algorithm and the governing equations-solver used are same as those in previous problem. The steady state governing equations (continuity and momentum) have been solved explicitly. The boundary conditions include no slip condition at walls and fully developed velocity profile at the inlet. The assumptions made in the numerical simulation are similar to those made in the previous problem. These include rigid arterial wall, incompressible, steady, laminar and Newtonian flow. The diameter/size of the idealized artery is large enough to consider the flow as Newtonian, since shear rate will be above 100 s^-1 for such dimensions. The steady blood flow simulation has been carried out for five different Reynolds numbers (120, 240, 480, 960 and 1920). Figure 7.1 shows the mesh with boundary layer elements. In order to overcome the pressure oscillation difficulties, safety factor (also known as relaxation factor) used is 0.5. The pseudo iterations were performed until the L2-norm of velocity and pressure errors reached 10^{-5} for all the Reynolds numbers. The solution converged at a mass error less than 0.3 % for all the Reynolds numbers.

7.3 Results and discussions

1. Figure 7.2 depicts vectorial representation of axial flow in the symmetric plane.

2. Three sections have been selected for qualitative studies of secondary flow. The three sections are shown in Figure 7.3. If the observer is visualizing the top view, left side of the section is towards internal curvature of the first bend. The numbering of the sections start from top of the artery, third one being the bottom most section. Figures 7.4 and

7.5 show secondary flow in the selected sections at Re-120 and Re-1920.

3. The pressure distribution for Re-120 and Re-1920 has been shown in Figure 7.6.

4. The wall shear stress contour plots at Re-120 and Re-1920 are given in Figure 7.7 .

5. In order to understand the spatial variation of WSS in the bend-type artery, WSS at four different geometrical entities has been give in the Table 7.2.

6. The graph in the Figure 7.8a gives the variation of WSS along the right hand side-edge of the artery. 20 points have been selected to plot quantitative distribution of WSS along the edge. First two points lie on the straight inlet, next six lie on the first bend, ninth one lies in between first and second bends, next 8 points are on the second bend and last three are on the outlet. Same order applies for the left hand side of the edge given in the Figure 7.8b.

7. The values of pressure and peak WSS at five different Reynolds numbers are given in Table 7.1.

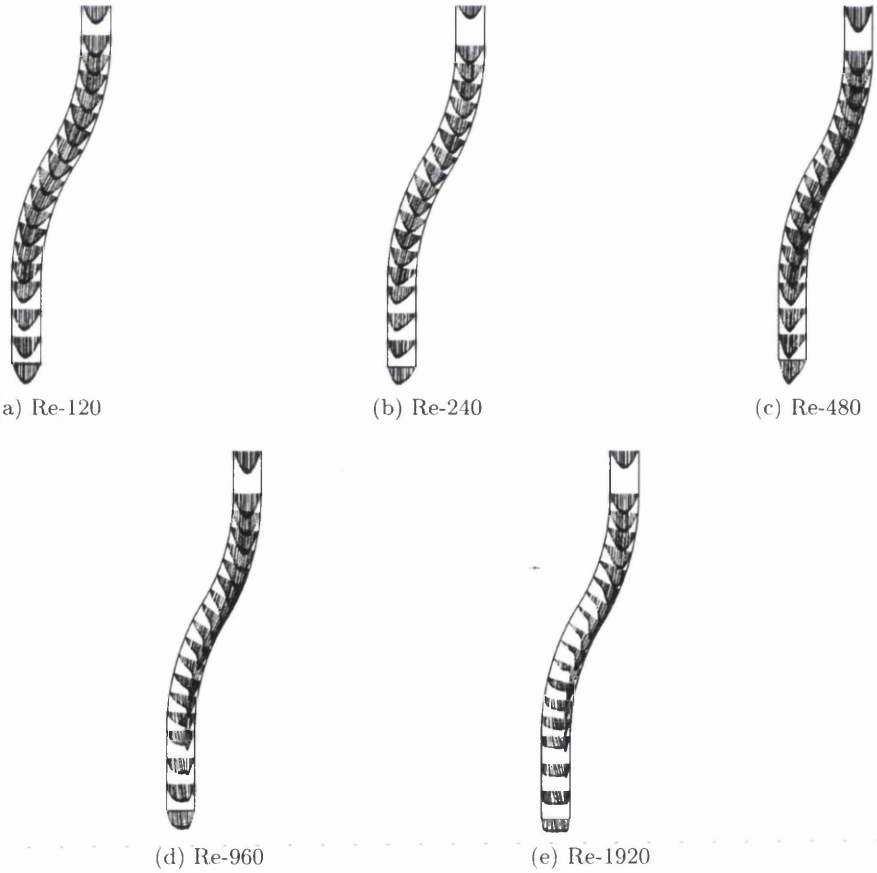

(a) Re-120 (b) Re-240 (c) Re-480

(d) Re-960 (e) Re-1920

Figure 7.2: An artery with two mild curvatures: Velocity vector in a symmetric plane (X-Z).

7.3.1 Flow in symmetric plane

From Figure 7.2, it can be noted that axial velocity is changing significantly with Reynolds numbers. However, at the lowest Reynolds number (i.e. 120), the flow appears parabolic at all the cross sections, indicating negligible impact of centrifugal load on the bends at this Reynolds number. In the first bend, the maximum of axial velocity is always concentrated towards external curvature (due to the higher centrifugal effect) for all the Reynolds numbers except Re-120. But for second bend, the path is highly dependent on Reynolds number. At lower Reynolds numbers the maximum of axial velocity is occurring towards the external curvature, due to the dominance of centrifugal effect over inertia effect. But for higher Reynolds numbers, the maximum of axial velocity is shifting drastically, towards internal curvature. This indicates that inertia forces dominate over centrifugal force at faster blood flow. The shifting of peak axial velocity away from the center of artery indicates flow separation. Because of this flow separation, the endothelium will experience high and low shear stresses. Axial velocity vector plots for all the Reynolds numbers are found to be matching with those obtained by *Hoogstraten et al* [19]. No double peaked axial flow has been observed in the first bend. This indicates that the double spiral vortex is not possible anywhere proximal to the first bend. The double peaked axial flow is a consequence of interaction between early bend-effect and the centrifugal force. The centrifugal load responsible for the formation of double peaked axial flow is believed to be nullified at the end of the first bend, due to the immediate presence of reverse curvature second bend [77]. A clear double peaked axial flow can be observed at the beginning of second bend. This happens due to the interaction between early second bend effect and centrifugal effect. The outflow profile at the highest Reynolds number resembles a blunt-turbulent velocity profile.

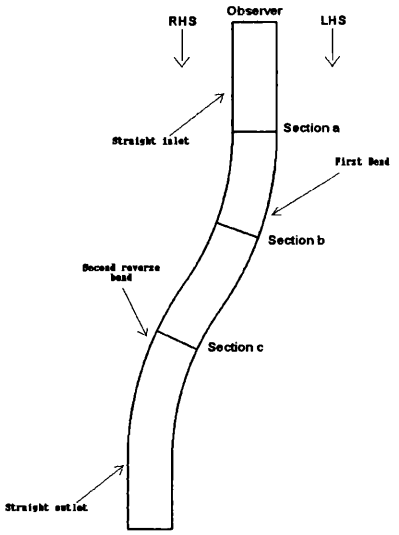

Figure 7.3: An artery with two mild curvatures: Three sections and an observer's view.

7.3.2 Secondary flow in sections

Due to the presence of boundary layer mesh, velocity vectors are close to each other near boundary in the Figures 7.4 to 7.5. In the section-a the secondary flow towards internal

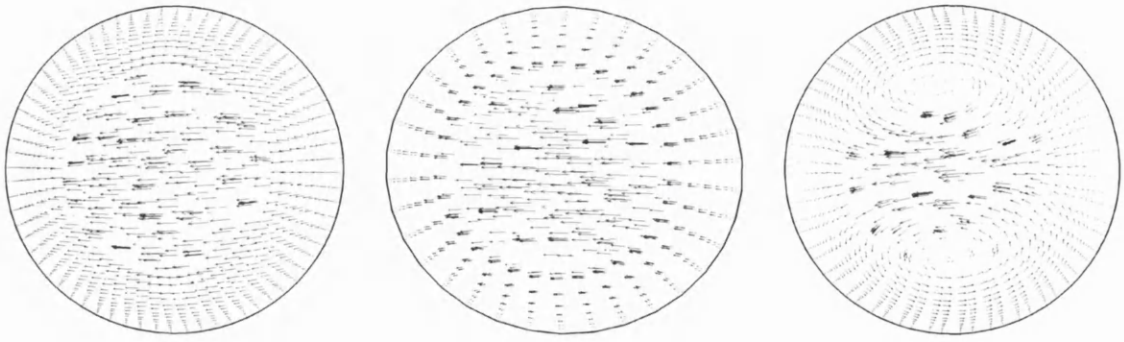

(a) Section a (b) Section b (c) Section c

Figure 7.4: An artery with two mild curvatures: Secondary flow in three cross sections (X-Y plane) at Re-120.

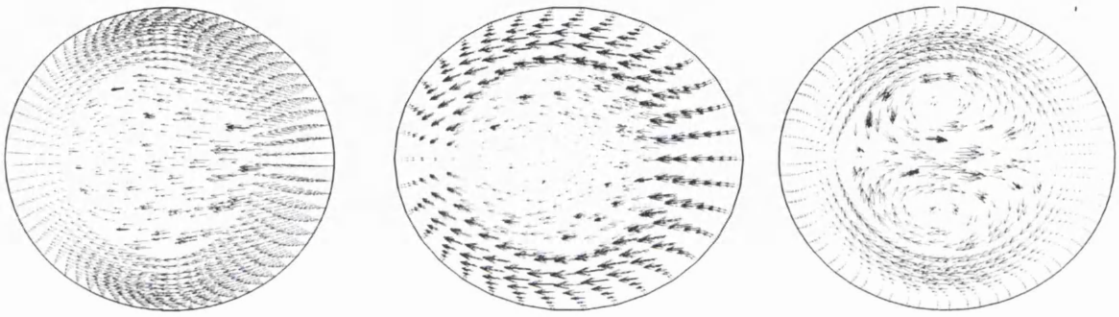

(a) Section a (b) Section b (c) Section c

Figure 7.5: An artery with two mild curvatures: Secondary flow in three cross sections (X-Y plane) at Re-1920.

curvature is found to be as high as 40 % (at Re-1920) of the primary flow. Indicating stronger early first bend effect. The percentages for sections b and c are 43 % and 20 % respectively. This proves that secondary flow due to early first bend effect diminishes over length of the artery. Similar to the the flow in a single bend, secondary flow at the middle of first bend is directed towards its internal curvature. This tendency of flow towards internal curvature is termed as early first bend effect. The early first bend effect occurs as a result of inertial dominated flow. Interestingly, there is no vortical formation in any cross section of the first bend, since the early first bend effect dominates over the centrifugal effect throughout the first bend. Secondary flow patterns are deviating from those obtained by *Hoogstraten et al* [19], since the vortices are being detected at the end of second bend only. But the flow pattern is found to be similar to those reported by *Banerjee et al* [77]. The centrifugal load responsible for the formation of complicated secondary flow is believed to be nullified at the end of the first bend, due to the immediate presence of reverse curvature second bend [77]. In the second bend, until the end of bend, the secondary flow is directed towards external curvature. This is due to the presence of early first bend effect in the second bend. Two recirculations can be clearly seen at the end of bend. This happens, since stronger centrifugal load required to drive the fluid particles to external curvature occurs at this cross-section. But at very higher Reynolds number (i.e. 1920), a weak vortex can be observed at the middle section of the second bend,

since at this Reynolds number, the strength of centrifugal force is enough to produce a small vortex before the end of second bend. Unlike a single bend artery in the previous chapter, more than two vortices cannot be found even at higher Reynolds numbers. This indicates that the secondary flow largely depends on angle of curvature of the bend and number of bends. The centrifugal load due to mild curvature is not strong enough to produce more than two vortices. The two vortices appearing downstream, change their direction of rotation at higher Reynolds number. At lower Reynolds numbers, the upper vortex is turning clockwise. Whereas, at higher Reynolds number (i.e. 1920) the upper vortex is turning anticlockwise. The presence of straight section between two bends may change the flow behavior, significantly. The presence of this intermediate straight section will result in stronger secondary flow at the end of first bend and it may also facilitate the presence of more than two vortices at the end of second bend. The element size plays a key role in capturing more accurate velocity vectors. Further refinement in the region other than boundary may show recirculating flow in the cross sections other than those observed here. Due to computational time constraints, this effort has not been considered in the present work.

7.3.3 Pressure distribution in the artery

At a lower Reynolds number (i.e. 120), the qualitative pressure distribution (Figure 7.6a) is roughly same as that of a single bend and straight arteries in previous chapters. But at higher Reynolds number (i.e. 1920), the peak pressure (Figure 7.6b) shifts to the junction of first-second bend. This indicates the presence of stronger early first bend-effect in this region and at the Reynolds number 1920. This region of wall at the junction is subjected to higher pressure due to the impingement of fluid particles driven by early first bend effect (refer the flow pattern in the Figure 7.2). The pressure drop is same as the maximum pressure, since the exit pressure is zero. At a given Reynolds number, the pressure drop value (refer Table 7.1) is found to be higher than that of the single bend artery (refer Table 6.1 in the previous chapter). This observation gives a clue that, pressure drop increases with increase in number of bends. Since the increase in number of bends increases the frictional loss. However the angle of curvature in these bends is smaller than that of the bend in the previous chapter. We will elucidate the effect of angle of curvature on the pressure distribution in the next chapter. The pressure plots in this analysis are found to be similar to those obtained by *Hoogstraten et al* [19].

Table 7.1: An artery with two mild curvatures: Results (dynes/cm^2) for five Reynolds numbers.

Re	Maxpressure	Pressuredrop	Peak WSS
120	93.7	93.7	2.65
240	194.2	194.2	7.2
480	430.3	430.3	22.1
960	1062.4	1062.4	65.3
1920	2512.773	2512.773	177.0

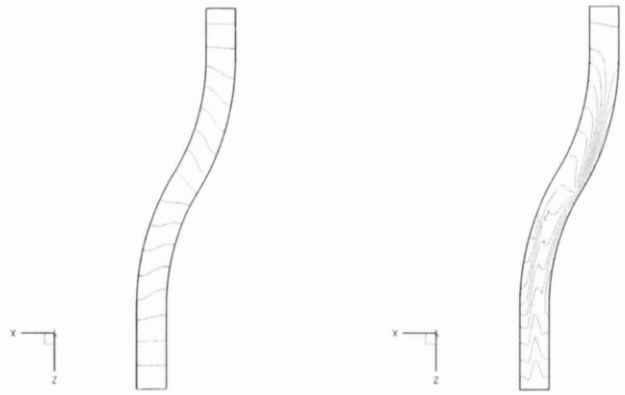

(a) Pressure distribution in symmetric plane-Re120.

(b) Pressure distribution in symmetric plane-Re1920.

Figure 7.6: An artery with two mild curvatures: Pressure distrubution (Peak values are given in Figure 7.1) .

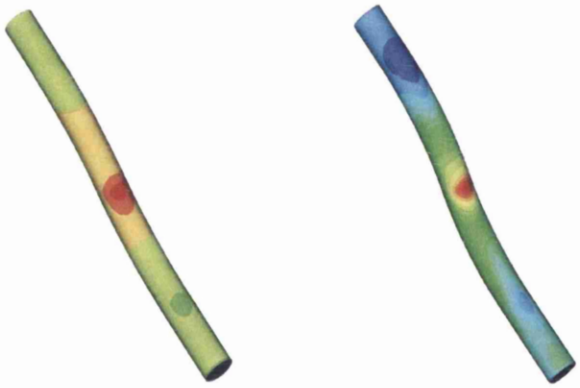

(a) WSS distribution-Re120

(b) WSS distribution-Re1920

Figure 7.7: An artery with two mild curvatures: WSS distribution (Peak values are given in Figure 7.1).

Table 7.2: An artery with two mild curvatures: Peak wall shear stress (dynes/cm^2) at five sections.

Re	Inlet	First bend	Intermediate region	Second bend	Outlet
120	2.25	2.27	2.65	2.192	2.055
240	5.35	5.785	7.2	5.775	4.955
480	11.22	14.0	22.1	13.3	9.455
960	25.55	35.44	65.3	42.245	20.15
1920	40.2	78.6	177.0	106.15	42.5

7.3.4 Wall shear stress

A WSS concentration region has been located at the external curvature of the first bend. This region is coincident with the junction between first and second bend. This remains same for

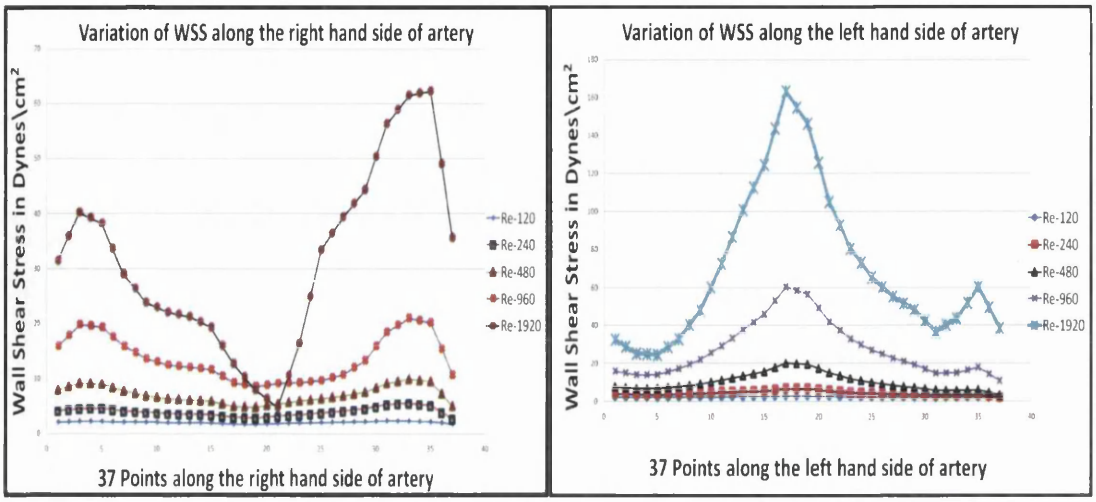

(a) Right hand side (b) Left hand side

Figure 7.8: An artery with two mild curvatures: Variation of wall shear stress along the edges of the artery.

all the Reynolds numbers. Due to mild curvature of first bend, the inertia effect dominates the centrifugal load resulting in shearing of fluid particles on the junction. The peak WSS value varies with the Reynolds number. For lower Reynolds numbers (i.e. 120 and 240), another small concentration region has been observed at the external curvature of second bend (view not shown here). The centrifugal effect seems to be strong enough in the second bend to produce little shearing of fluid particle on the external curvature of the second bend. The highest value of peak WSS observed is 177.0 dynes/cm^2, which happens at Reynolds number 1920. At a given Reynolds number, the peak WSS value is found to be slightly higher than that of the single bend artery in the previous chapter. This observation gives a clue that, peak WSS increases with number of bends. This slight difference in shear stress is also due to the milder curvature of the bends. By observing the Table 7.2, we can conclude that the first-second bend junction is subjected to higher WSS and straight outlet section is subjected to lower WSS. Physiologically, we can also conclude that any straight luminal region proximal to the bend is vulnerable for plaque accumulation. The magnitude of WSS in the straight inlet region is found to be closer to that of Poiseuille's shear stress calculated for flow through a straight artery (refer Table 5.1 of Chapter 5). This validation has been confirmed for all the Reynolds numbers (Table 7.2). However a slight difference occurs, which is due to early-first bend effect. The presence of bend next to a straight inlet, increases the WSS in the inlet. At lower Reynolds numbers (Re-120 and Re-240) the straight outlet appears to regaining the poiseuille's WSS. But at higher Reynolds numbers, the magnitude of WSS in the straight outlet deviates significantly from poiseuille's WSS, Since centrifugal effect experienced by bends prevail downstream in the straight outlet. Highly distorted outflow profile at higher Reynolds number-flow (Figure 7.2) is the evidence for this effect in the straight outlet. By observing the graphs in the Figure 7.8, we can conclude that the left hand side-edge is subjected to higher shear stress and the right hand side-edge experiences relatively lower shear stress. This is a consequence of higher axial flow along the left hand side-edge (refer Figure 7.2). The abrupt spatial variation of WSS occurs at higher Reynolds numbers only. Along the left hand side-edge of the artery, the wall shear stress raises gradually until the end of first bend and

drops gradually along the second bend. This gradual decrease of WSS occurs, since the flow is slightly directly away from the wall at the end of second bend. The WSS along the left hand side-edge of the outlet increases to 60 dynes/cm^2 (Re-1920), due to turbulent type flow profile. The WSS along the right hand side of the artery drops until the end of first bend and raises until a location proximal to the end of the second bend. Interestingly, at very high Reynolds number (1920), the WSS at the location where internal curvature of the first bend meets the external curvature, drops to a value lesser than that of Re-960. This dip in WSS occurs, since much of the fluid particles speeding under the influence of inertia (late first bend effect) are driven towards the internal curvature of the second bend, and very few of them will shear the opposite wall. In both the graphs, the WSS start with a value approximately closer to the Poiseuille WSS (refer Table 5.1 of Chapter 5). By these graphs we can also conclude that the inner curvature of the first bend and external curvature of the second bend experience lower WSS as compared to their opposite walls and these walls are susceptible for atherogenesis. According to the graph, the WSS at the end of the external curvature of the first bend reaches as high 160 dynes/cm^2 (at Re-1920). We can hypothesize that this large value of WSS might initiate the damage of endothelial cells.

Chapter 8

Flow in a model artery with two bends of 90 degree each

8.1 Introduction

A double curved artery with constant diameter (D) has been considered for numerical simulation. The length of the straight inlet section is 5D. There are two bends in the artery. The radius and angle of curvature of the inlet curved bend are 5.833D and 90 degree respectively. The radius and angle of curvature for the outlet curved bends remains same as that of inlet bend. The curvature of bends in this example is stronger than the bends in the previous chapter. This strong curvature will induce the abnormal flow pattern, higher intensity of flow separation and abrupt wall shear stress distribution. Such haemodynamical anomalies in a weakened artery will lead to pathologies such as arterial lesions, thrombosis and hyperplasia. Physiologically, angle of curvature can be as high as 180 degree. Typical examples include aortic arch and intracranial region of internal carotid artery [38]. The Reynolds numbers selected are 120, 240, 480, 960 and 1920. This analysis is based on the research done by. Similar to the double bend artery in the previous chapter, the two curvatures are in the same plane of symmetry and the planes of inlet and outlet are parallel to each other. In order to validate the solution, the geometrical features chosen here are based on the research work conducted by *Qiao et al* [24]. The main objective of this chapter is to explore the qualitative and quantitative primary/axial flow, secondary flow patterns, wall shear stress and pressure in an artery with two strong curvature-bends. Similar to the artery in the previous chapter, in order to understand the flow behavior in various sections of the artery, the spatial domain can be divided in to four entities. These entities are straight inlet, first bend, second reverse-bend and straight outlet. We will discuss about the flow pattern in all these sections. The value of WSS in the straight inlet is found be in good agreement with analytical solution (Poiseuille flow). This agreement serves as a validation of mesh and the CFD code. This double bend artery has been solved for two cases:

- Case-I: Lumen Diameter D= 0.6 cm
- Case-II: Lumen Diameter D= 1.2 cm

The ratio (k_c) of vessel radius to curvature radius is 0.086 and 0.171 for case-I and case-II respectively. The non dimensional dean numbers from the Equation 3.1 (at Re-1920) are 563 and 793.4 for case-I and case-II respectively. These two case studies are intended to understand the relation between flow patterns and the luminal radius. The artery with smaller diameter (D = 0.6 cm) represents minor arteries such as coronary artery. Whereas the artery with higher radius (0.6 cm) represents large arteries such as aorta. The luminal radius is an influential factor on wall shear stress and wall pressure. In the present work, it has been found that the increase of radius results in reduction of pressure drop ($\Delta P = 8\mu u_{avg} l Q/\pi r^4$) and wall shear stress ($\tau_{wall} = 4\mu Q/\pi r^3$).

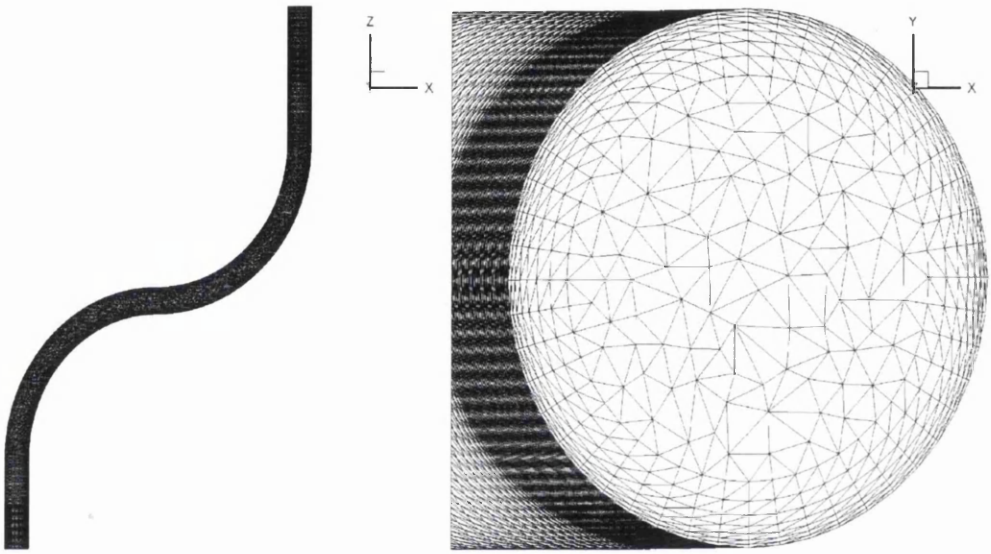

(a) Surface mesh (b) Cross-sectional view of the mesh

Figure 8.1: An artery with two strong curvatures: Meshed model.

8.2 Numerical model and boundary conditions

The finite element grid with boundary layers consisted 120814 elements and 211010 nodes for case-I. The finite element model for case-II consisted of 1255330 elements and 216822 nodes. For both the cases, average element size in the model is 0.03 cm and number of boundary layers is eight. The mesh is of uniform longitudinal spacing and thickness of the edge boundary layer is 0.002 cm for both the cases. The total boundary layer thickness is 0.077 cm and number of boundary layers is 8 for both the cases. The mesh generation algorithm and the Navier-Stokes equation solver used are same as those in previous problem. The boundary conditions include no slip condition at walls and fully developed velocity profile at the inlet. The assumptions made in the numerical simulation are similar to those made in previous problem. These include rigid arterial wall, incompressible, Newtonian, homogenous, steady and laminar flow. The density and viscosity of the blood are 1050 kg/mm^3 and 0.04 poise respectively. The model has been built in cartesian coordinate system (x, y, z). w is the axial velocity and it represents primary flow. u is the velocity in the plane of curvature and v is the velocity component perpendicular to the plane of symmetry. The combination of u

and v (i.e. $\sqrt{u^2+v^2}$) represents secondary flow. The steady blood flow simulation has been carried out for five different Reynolds numbers (120, 240, 480, 960 and 1920). Figure 8.1 shows the mesh with boundary layer elements. In order to overcome the pressure oscillation difficulties, safety factor used is 0.5. The pseudo iterations were performed until the L2-norm of velocity and pressure errors reached 10^{-5} for both the cases and all the Reynolds numbers. The solution converged at a mass error less than 0.3 % for both cases and all the Reynolds numbers.

8.3 Results and discussions

1. Figures 8.2 and 8.3 depict vectorial representation of flow in the symmetric plane for case-I and case-II respectively.
2. six sections have been selected for qualitative studies of secondary flow. The six sections are shown in Figure 8.4. Left side of the sections is towards internal curvature of the first bend. The numbering of the sections start from top of the artery, sixth one being the section proximal to the outlet. Figures 8.5 and 8.6 represent secondary flow in selected six selections at Re-1920.
3. The pressure distribution at Re-120 and Re-1920 has been shown in Figures 8.7 and 8.8 for case-I and case-II respectively.
4. The graph in the Figure 8.9a gives the variation of WSS along the right hand side-edge of the artery. 17 points have been selected to plot quantitative distribution of WSS along the edge. First three points lie on the straight inlet, next five lie on the first bend, ninth one lies in between first and second bends, next five points are on the second bend and last three are on the outlet. Same order applies for the left hand side of the edge given in the Figure 8.9b.
5. The wall shear stress contour plots at Re-120 and Re-1920 are given in Figures 8.10 and 8.11 for case-I and case-II respectively.
6. In order to understand the spatial variation of WSS in the bend-type artery, WSS at four different geometrical entities has been give in the Tables 8.3 and 8.4 for case-I and case-II respectively.
7. The values of peak pressure, pressure drop and peak WSS at five different Reynolds are given in Tables 8.1 and 8.2 for case-I and case-II.

8.3.1 Flow in symmetric plane

From Figures 8.2 and 8.3, it can be noted that axial velocity is changing significantly with Reynolds numbers for both cases. At lower Reynolds number (i.e. 120), the flow remains developed at the outlet for case-I. But for case-II, the outlet flow is asymmetric even for lower Reynolds number (i.e. 120), since the late second bend effect prevails downstream to the straight outlet. At all the Reynolds numbers and both the cases, the maximum of axial velocity in the first bend is pushed towards the external radius of the bend. This indicates the presence of centrifugal effect in the first bend. In the first bend, flow tends to separate

Table 8.1: An artery with two strong curvatures: Results (dynes/cm^2) for five Reynolds numbers-Case-I.

Re	Maxpressure	Pressuredrop	WSS
120	183.0	183.0	2.54
240	372.0	372.0	7.165
480	853.72	853.72	18.7
960	2126.05	2126.05	50.25
1920	5963.0	5963.0	168.7

Table 8.2: An artery with two strong curvatures: Results (dynes/cm^2) for five Reynolds numbers -Case-II.

Re	Maxpressure	Pressuredrop	Peak WSS
120	102.65	102.65	1.933
240	229.025	229.025	5.4
480	525.6	525.6	14.66
960	1454.326	1454.326	49.44
1920	4418.459	4418.459	157.02

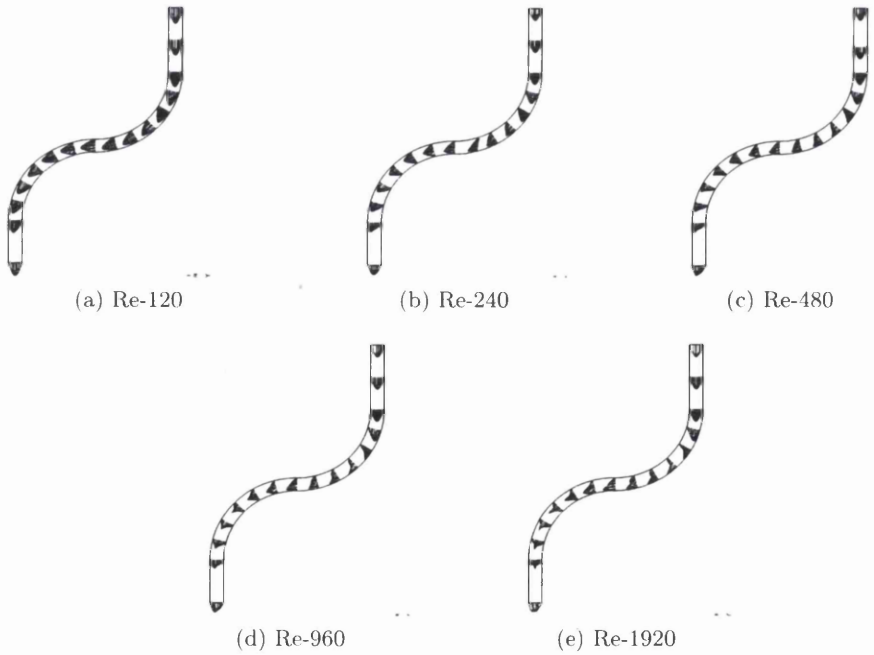

(a) Re-120 (b) Re-240 (c) Re-480

(d) Re-960 (e) Re-1920

Figure 8.2: An artery with two strong curvatures: Velocity vectors in symmetric plane (X-Z plane) for Case-I.

from internal curvature and concentrate towards external curvature, resulting in higher shear stress on the external curvature wall and lower shear stress on the internal curvature wall. Same trend appears in the second bend of case-I. The axial flow in the second bend is highly

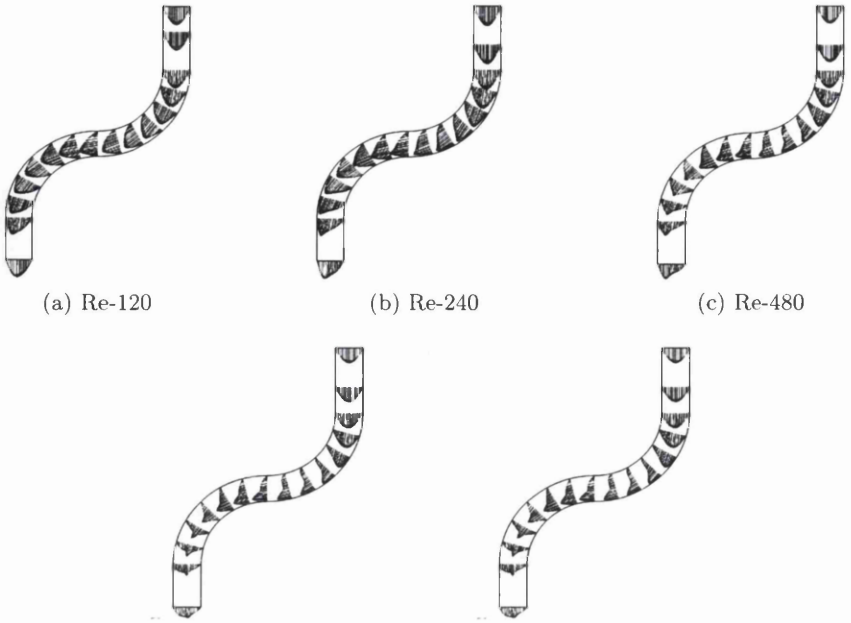

(a) Re-120 (b) Re-240 (c) Re-480

(d) Re-960 (e) Re-1920

Figure 8.3: An artery with two strong curvatures: Velocity vectors in symmetric plane (X-Z plane) for Case-II.

dependent on radius of vessel. For case-I, the maximum of the axial velocity in the second bend is fully concentrated towards the external radius. But flow pattern in second bend is different for case-II. For case-II, the maximum of axial velocity in the second bend is found to be at the center of the vessel. But the flow in the second bend of case-II (Re-960 and Re-1920) is asymmetric. In the early phase of the second bend, the flow is relatively higher near internal curvature due to late first bend effect. At the end of bend, the flow is relatively higher towards the external curvature, since the centrifugal effect dominates the late first bend effect. A comparison can be done with case-I and the artery in the previous chapter, since the lumen diameter remains same. The comparison indicates that the axial velocity in the second bend is completely different. Thus, the axial velocity in the second bend is highly dependent on the angle of curvature of the bend. In the previous chapter, the early first bend inertia effect prevailed downstream to the artery due to mild curvature. This resulted in shifting of axial flow towards internal curvature of the first bend. Whereas higher centrifugal effect due to stronger curvature pushed the flow towards external curvature of second bend in case-I artery. Flow separation can be clearly observed in the curvatures of both bends (Figures 8.2e and 8.3e). These flow separation regions will induce extremum of wall shear stress gradient. Unlike the artery of previous chapter, turbulent type blunt outflow profile has not been observed at higher Re numbers here. Occurrence of turbulence is unlikely here, since the centrifugal effects due to stronger curvature dominate the inertia effects.

8.3.2 Secondary flow in sections

From the Figures 8.5 and 8.6 it is clear that, secondary flow is stronger downstream for both cases and at all the Reynolds numbers. No recirculation occurs in the first bend. The secondary

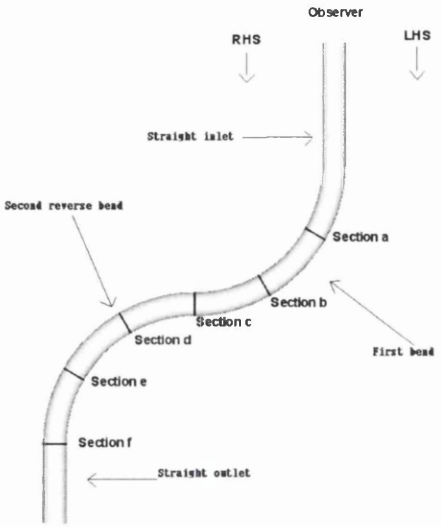

Figure 8.4: An artery with two strong curvatures: Six sections chosen in the double bend artery and an observer's view.

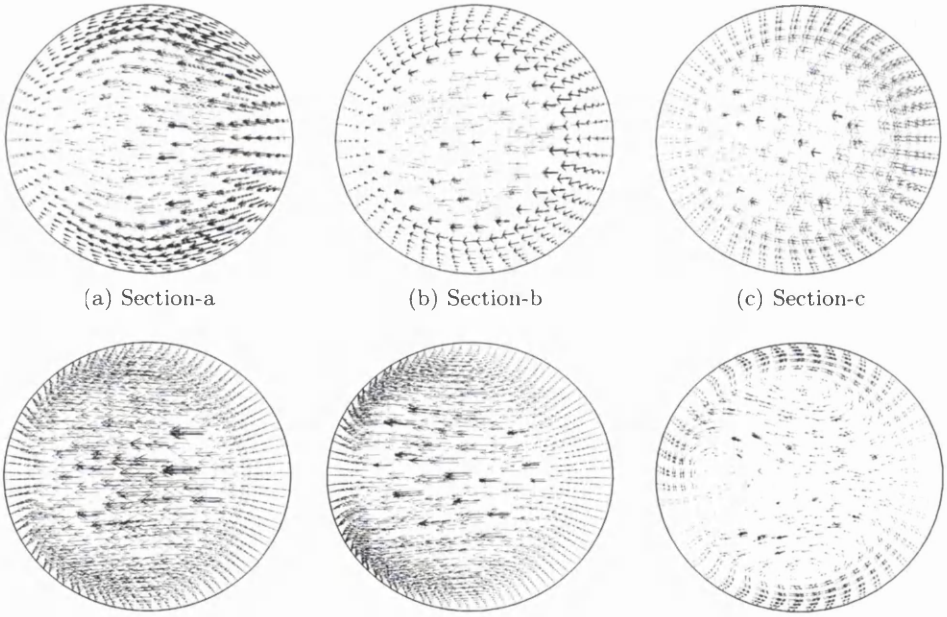

(a) Section-a (b) Section-b (c) Section-c

(d) Section-d (e) Section-e (f) Section-f

Figure 8.5: An artery with two strong curvatures: Secondary flow in all six sections (X-Y plane) at Re-1920-CaseI.

flow in the first four sections is always directed towards the internal curvature of the first bend, since the early first bend effect dominates the centrifugal effect in the first bend. Whereas the secondary flow in the next three sections is directed towards external curvature. This indicates that early first bend effect prevails even in the second bend. If a secondary flow comparison is made between case-I and case-II, there are observable differences. For case-II, the formation

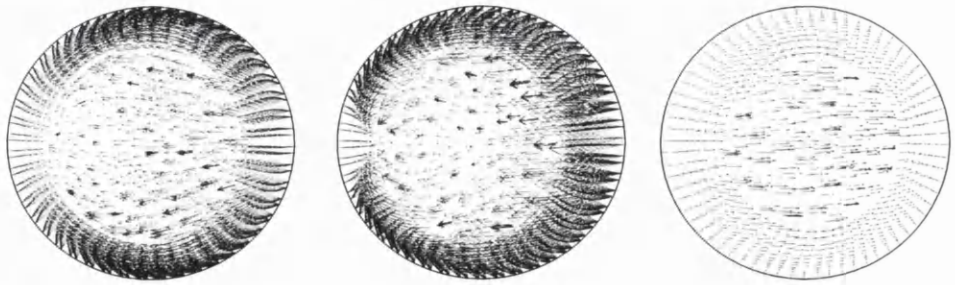

(a) Section-a (b) Section-b (c) Section-c

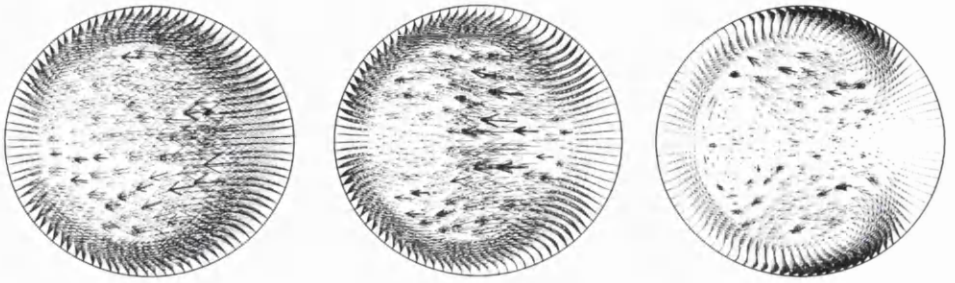

(d) Section-d (e) Section-e (f) Section-f

Figure 8.6: An artery with two strong curvatures: Secondary flow in all six sections (X-Y plane) at Re-1920-CaseII.

of four vortices downstream occurs at Reynolds number-480 (figure not shown here). But the number of vortices observed for the case-I at the same Reynolds number is two (figure not shown here). In case-II, more than two vortices can be seen at Re-960 (figure not shown here). Thus, the strength of the secondary flow depends on radius of the lumen. This fact is in accordance with Dean number given by Equation 3.1 of Chapter 3. In the first section the secondary flow (calculated using $\sqrt{u^2+v^2}$, where u and v are components perpendicular to the axial flow w) is found to be 50 % of primary flow, indicating the dominance of secondary flow in the first bend. At the junction of first-second bends, secondary flow is found to be six times higher than that of primary flow. since the dominance of secondary flow over primary is very high. The secondary flow u (component in the plane of curvature), is as high as ten times of that of primary velocity, due to the first bend centrifugal effect. The multiple vortical secondary flow will not occur at this junction, since the centrifugal effect will be nullified by the immediate presence of reverse curvature second bend. At the end of second bend, the secondary flow is found to be 12 % of primary flow. This Indicates that the primary flow dominates the secondary flow at downstream of the artery. This percentage wise combination of secondary-primary flows is found to be similar for both the cases. Secondary flow with multiple vortices can be observed downstream to the second bend only. This secondary flow pattern occurs since the fluid particle driven by late second bend effect will be centrifugally pushed to the external curvature.

8.3.3 Pressure distribution in the artery

At a lower Re (i.e.120), the qualitative pressure distribution (Figure 8.7a) in the case-I artery is approximately same as that of a double bend, single bend and straight arteries studied in

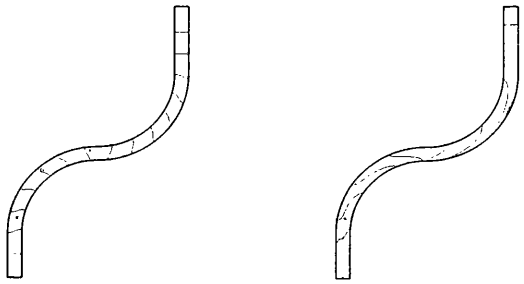

(a) Re-120 (b) Re-1920

Figure 8.7: An artery with two strong curvatures: Pressure distribution for Case-I (Peak values are given in Table 8.1) .

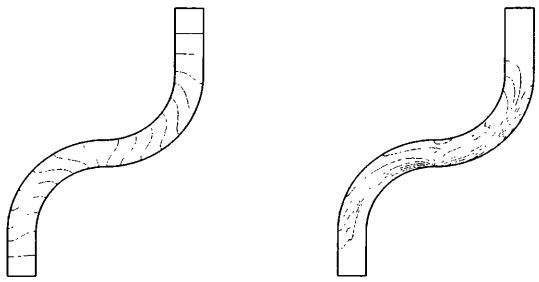

(a) Re-120 (b) Re-1920

Figure 8.8: An artery with two strong curvatures: Pressure distribution for Case-II (Peak values are given in Table 8.2).

the previous chapters. But it varied significantly for case-II. In case-I, peak pressure remains at the inlet for all the Reynolds numbers (Figure not shown here except for Re-120 and Re-1920 in Figure 8.7), indicating lower centrifugal effect on pressure for smaller luminal radius. But in the case-II, peak pressure shifts to the external curvature of the first bend at Re-480 and above. This is happening due to the stronger impact of fluid particles on the the curved wall, induced by higher mass flow rate. This effect has also been observed in the single bend problem of Chapter 6. For the single bend artery, this impact on the curved wall of bend occurred at Re-960. But in case-II, the impact appeared at Re-480, due to higher flow rate. From Tables 8.1 and 8.2, it is clear that peak pressure and pressure drop are lower in case-II. Larger luminal radius decreases the pressure drop ($\Delta P = 8\mu u_{avg} LQ/\pi r^4$). In both the cases, pressure drop increases with the Reynolds number. Pressure values of Case-I can be compared with the artery analyzed in the previous chapter, since the luminal radius remains same. The peak pressure and pressure drop values in the case-I are found to be higher than those of the arteries presented in the previous chapter. This indicates that, the pressure drop and peak values increases with the angle of vascular curvature. The change in radius of curvature modifies the spatial pressure distribution. In the previous chapter higher pressure concentration (at Re-480 and above) occurred at the curvature wall, since the radius of curvature was relatively higher ($r_c = 3.9$ cm). But in this chapter (case-I), the highest pressure occurs at the inlet for all the Reynolds numbers. Since smaller centrifugal effect occurring due to smaller radius of curvature ($r_c = 3.5$ cm) is not enough to pressurize the curvature wall.

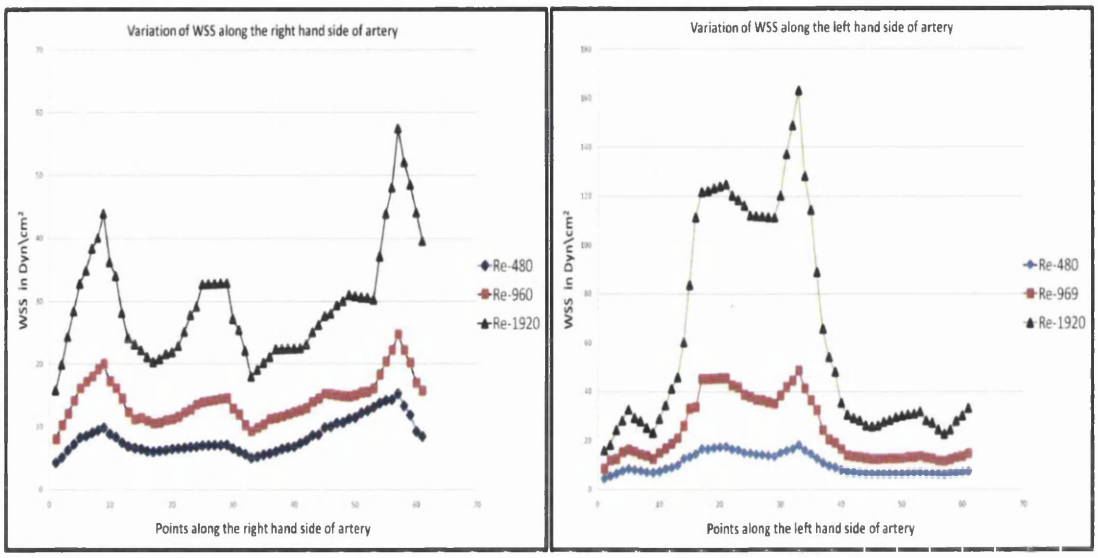

(a) Right hand side (b) Left hand side

Figure 8.9: An artery with two strong curvatures: Variation of wall shear stress along the edges of the artery (case-I).

(a) Re-120 (b) Re-1920

Figure 8.10: An artery with two strong curvatures: WSS distribution for Case-I (Peak values are given in Table 8.3).

Table 8.3: An artery with two strong curvatures: Peak wall shear stress (dynes/cm^2) at six sections for case-I.

Re	Inlet	First bend	Intermediate region	Second bend	Outlet
120	2.745	2.255	2.54	2.45	2.01
240	4.175	4.585	7.165	4.95	4.905
480	9.0	14.0	18.7	12.8	12.0
960	17.55	32.75	50.25	34.95	34.45
1920	39.3	131.685	168.7	134.7	131.5

8.3.4 Wall shear stress

For the case-I, WSS is found to be concentrated at the end of first bend for Re-120 and Re-240 (Figure not shown here), since the presence of immediate reverse curvature second bend causes

(a) Re-120 (b) Re-1920

Figure 8.11: An artery with two strong curvatures: WSS distribution for Case-II (Peak values are given in Table 8.4).

Table 8.4: An artery with two strong curvatures: Peak wall shear stress (dynes/cm^2) at six sections for case-II.

Re	Inlet	First bend	Intermediate region	Second bend	Outlet
120	1.35	1.625	1.93	1.635	1.48
240	2.88	4.5	5.35	4.5	4.255
480	6.35	12.665	14.55	12.6	9.8
960	15.3	41.55	49.2	41.2	28.05
1920	31.5	136.2	156.75	136.2	77.2

the fluid particle to shear the wall at the junction. For higher Reynolds numbers (480 and above), peak WSS is also found at the external curvature of first bend, since the centrifugal load due to higher velocity impinges the fluid particle on this wall. For case-II, peak WSS is found to be at the end of first bend for all the Reynolds numbers, since lower centrifugal effect due to higher luminal radius (refer Equation 6.1) is not enough to impinge fluid particles on the first bend and reverse curvature second bend shears the fluid on the junction wall. From Tables 8.1 and 8.2, it is evident that WSS is higher in the case-I artery for all the Reynolds numbers than case-II. Thus, the WSS depends on the lumen diameter and it is higher for an artery with smaller lumen diameter ($\tau_{wall} = 4\mu Q/\pi r^3$). By this observation, it can be hypothesized that, the narrowing of lumen due to atheroma will lead to higher WSS on the walls. WSS values of Case-I can be compared with the artery analyzed in the previous chapter, since the lumen radius remains same. Peak WSS for the artery with 35 degree bend in the previous chapter occurred at the end of first bend, for all the Reynolds numbers. This is in contrast with the case-I, since the location of peak WSS has shown dependency on Reynolds number (peak WSS occurs at two locations at higher Re). Thus, the location of peak WSS in a bend-type artery depends on the angle of curvature. Lower angle of curvature results in direct impingement of particles on the first-second bend junction. Whereas the higher angle of curvature results in impingement (due to centrifugal effect) of fluid particles on the first bend external curvature wall. However the magnitude of centrifugal effect depends on the Reynolds number. The values of peak WSS at various Reynolds numbers for the 35 degree bend in the previous chapter are closer to those of case-I. Thus, the values of peak WSS is not found to be varying significantly with the increase in angle of curvature (from 35^0 to 90^0). However, further increase in angle of curvature (above 90^0) might vary the WSS significantly. From Tables 8.3 and 8.4, it is clear

that the intermediate region (junction between first-second bend) is subjected to higher WSS for both cases. It is worthwhile to perform unsteady simulation and examine OSI (oscillatory shear index) in this region. The peak WSS in the inlet is in good agreement with analytical calculations (refer Chapter 5 and compare with Case-I). At lower Reynolds numbers (120 and 240), the peak WSS in the outlet is closer to the analytical calculations. Whereas for higher Re (480 and above) the flow disturbances due to the presence of bends will not allow the flow to develop at the outlet, resulting in higher WSS. From the graph 8.9, it is clear that RHS and LHS experience totally different WSS patterns. The WSS at both sides starts with a value closer to poiseuille's WSS. In the LHS, the WSS increases to a peak value 162 dynes/cm^2, due to centrifugal effect on the external curvature of the first bend. Whereas, the WSS in the RHS decreases to a value lesser than that of poiseuille's flow. This drop in WSS at the internal curvature might initiate atherosclerosis and *Banerjee et al* [77] have observed lesions in this region. In the RHS, after this drop, the WSS oscillates and increases to a peak value 58 dynes/cm^2. This raise in WSS occurs at the end of second bend, due to presence of external curvature and the resulting centrifugal effect. In the LHS, once the WSS reaches peak value, it sharply drops to a value closer to that of poiseuille's flow. The same WSS pattern has been observed for RHS and LHS edges of case-II (Figure not shown here). By these observations, we can generalize that, in any bend-type arteries, internal curvature-walls are subjected to lower WSS and external curvature-walls are subjected to higher WSS. The resulting wall shear stress gradient between external and internal curvatures will play a vital role in vascular pathogenesis.

Chapter 9

Flow through a patient specific thoracic aortic aneurysm

9.1 Introductions to aneurysms

Aneurysm is an abnormal and local expansion of blood vessels. It occurs in response to weakening and disease of arteries. Aneurysms most commonly occur in arteries. In exceptional cases, aneurysms are also found in veins [49]. The arteries located in the circle of willis are most vulnerable for aneurysms. These aneurysms are known as cerebral aneurysms. An aorta can also be inflicted with aneurysms. The aortic aneurysms can be classified into thoracic aortic aneurysms (TAA) and abdominal aortic aneurysms (AAA). Other aneurysms are known as peripheral aneurysms. The aneurysms found in femoral, carotid and internal mammary [72] arteries are known as peripheral aneurysms. A growing aneurysm can rupture leading to death of the patient. The morbidity and mortality rates of AAAs in England are as high as 11,000 and 10,000 respectively, per year [71]. Diagnostic methods available to detect cerebral aneurysms are CT scanning, lumber puncture, cerebral angiography and computer tomographic angiography. The risk factors for pathogenesis of aneurysms include polycystic kidney disease, syphilis, diabetes, obesity, hypertension, tobacco use, alcoholism, marfan's syndrome and copper deficiency. A cerebral aneurysm is asymptotic until it ruptures. Symptoms of aneurysmal growth or ruptures include are drastic drop in blood pressure, rapid heart rate and light-headedness. Men are more likely to be diseased with aneurysms than women. Geometrically, aneurysms can be classified into pseudo, fusiform and saccular. A fusiform aneurysm is the expansion of whole cylindrical portion of a section of an artery. Whereas a saccular type involves bulging a side of an artery. In a pseudo aneurysm, the outer layer of an artery is enlarged. Histologically, aneurysms are due to intimal cell damage. Endothelial cells damage as a result of higher shear stresses by blood flow. Healthy cells are round in appearance, where as damaged cells appear elongated. Once an aneurysm has been formed, control of blood pressure is very significant. In this age of advanced medical technology, there are various treatment options available for aneurysms. Cerebral aneurysms can be treated either by surgical clipping or endo-vascular coiling. An aortic aneurysm is usually treated by grafts. Graft system can be introduced through a femoral artery and then driven to the aorta [8]. This method involves replacement of inflicted artery with a man made duct known as graft. Treatment of an aneurysm also involves medication. Medication can be done to reduce blood pressure, relax blood vessel and minimize the risk of rupture. Most commonly prescribed medicines are beta blockers and cal-

cium blockers. However, prevention is always better the cure. The occurrence of an aneurysm or any cardiovascular pathology can be prevented by teetotaling, cholesterol and fat dieting, controlling high blood pressure and carrying out physical exercise.

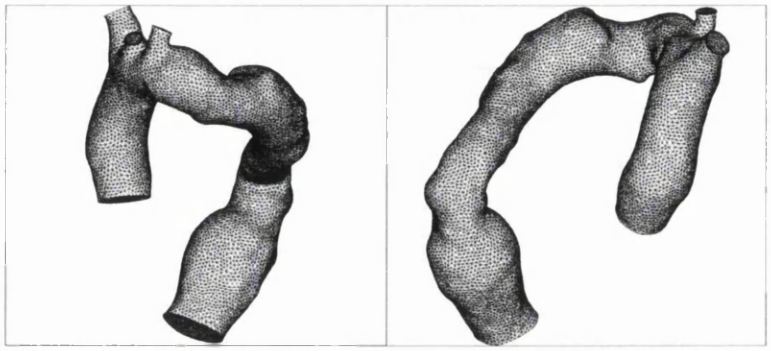

(a) Anterior view (b) Posterior view

Figure 9.1: TAA: Meshed model.

9.2 *In silico* modeling of a thoracic aortic aneurysm

Geometrical modeling of any human organ is extremely challenging. The presence of a folded neck in this aorta, makes the modeling and simulation more interesting. The modeling and simulation of flow through a realistic aorta will give better understanding of flow and wall shear stress patterns, which is not possible by simulating idealistic models. The geometry of the aorta inflicted with aneurysm has been constructed using CT-scans. The resolution of the scan is 0.0877x0.0877 cm in the slice plane and 0.1 cm between slices. Region segmentation has been done by *AMIRA*®. The stereolithiographic (STL) file generated by *AMIRA*® cannot be used directly to obtain a smooth mesh. The model obtained at this point, involves many small vessels attached to the main aorta. The small vessels, which are irrelevant to the present simulation have been clipped and removed. But small proximal parts of left subclavian, left common carotid arteries and brachycephalic trunk are retained. Mesh contraction method is used to obtain a smooth surface mesh [73]. Volume triangulation has been done by an in-house mesh generator known as FLITE3D. The anterior and posterior views of the mesh can be seen in the Figure 9.1. A bulge located at the bottom of descending aorta is the aneurysm. The algorithm in the mesh generator is based on triangulation method [23]. For more detailed explanation on geometrical modeling and grid generation, readers are referred to [74]. The approximate inlet diameter is 3 cm and approximate height (measured from outlet to the top of aortic arch) is 20.1 cm. The mesh consists of 75443 nodes, 420351 tetrahedrons-elements and five boundary layers, so that wall shear stress can be calculated accurately. The average element size of the finite element model is 0.08 cm. The approximate boundary layer thickness is 0.05 cm and final layer (layer adjacent to the wall) thickness is 0.003 cm. The boundary layer of three branch-outlets and the inlet can be seen in the Figure 9.2. The governing mass and momentum equations have been solved using CBS method (refer Chapter 4) to compute three dimensional velocities, wall shear stress distributions and pressure distributions. Unlike the steady state solution for the arteries in the previous chapters, this numerical model has been

solved for an unsteady flow. In order to overcome the pressure oscillation difficulties, safety factor used is 0.5. The pseudo iterations were performed until the L2-norm of velocity and pressure errors reached 10^{-5} for each time increment. The solution converged at a mass error less than 0.2 % for each time step. Just for the sake of curiosity, an unsteady flow simulation without the folded neck (by smoothing the neck geometry) has also been performed. In this case considerable differences in WSS and OSI distribution have been identified, as compared to the aorta with a realistic folded sharp neck.

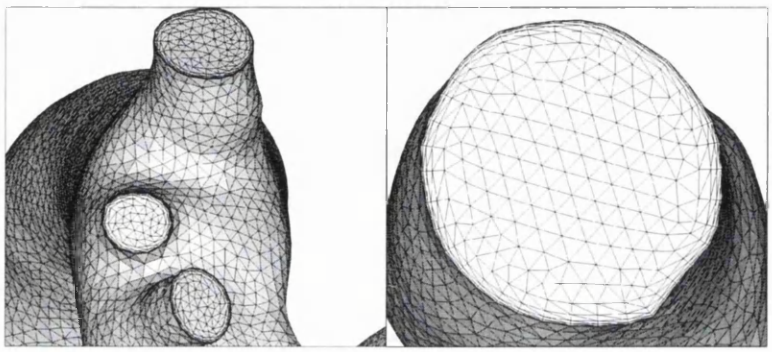

(a) Three branch outlets (b) Inlet

Figure 9.2: TAA: Boundary Layer Mesh.

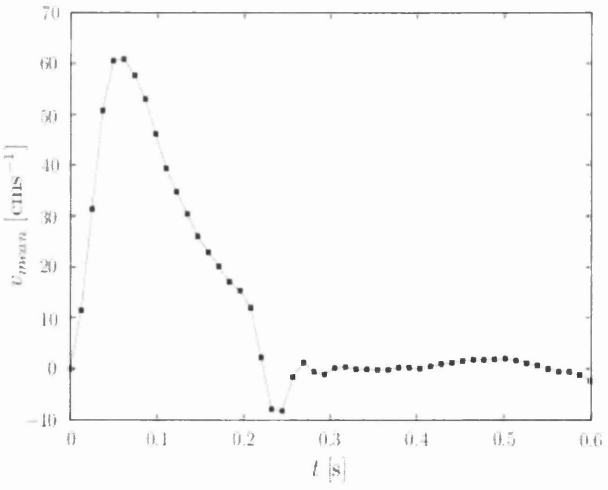

Figure 9.3: TAA: Temporal velocity waveform.

9.3 Boundary conditions

Similar to the problems in previous chapters, no slip condition has been enforced on walls. A fully developed-pulsatile waveform has been prescribed at the inlet and outlets. Since the inlet and outlet surfaces are not circular, *Hagen-poiseuille* flow given in the Equation 4.6 cannot

be implemented. For non-circular sections, *Hagen-poiseuille* flow needs to be mapped. This mapping procedure has been de described by *Mynard and Nithiarasu* [34]. This procedure involves computing the spatial variation of velocity by the equation:

$$u = 2u_{mean}(1 - r_{norm}^2) \tag{9.1}$$

where $r_{norm} = r/R_i$ is a normalized radius, r being the radius measured from the node and R_i is the radius measured from an imaginary node. Womersley profile described in the equation 2.2 cannot be used in this situation, since Womersley profile is applicable for cylindrical walls only. In order to obtain a pulsatile velocity profile in time, u in the above equation should be multiplied by a transient profile $k(t)$:

$$k(t) = \sum_{i=1}^{n_{harm}} B_i cos(\omega_i t + \phi_i) \tag{9.2}$$

where t is time, B_i is amplitude, $\omega_i = 2\pi f_i$ is angular frequency and ϕ_i is phase angle of ith harmonics. All these parameters are realistic in nature and have been obtained from hospital. The values for these parameters are presented in the Table 9.1. For comprehensive understanding about this data acquisition methodology, readers are referred to [34]. The temporal velocity of one cardiac cycle is shown in the Figure 9.3. The analysis of quickly changing flow (pulsatile) requires very small step sizes. Therefore, the temporal domain has been discretized into 99 steps, where one step size 0.006 second. The total time length of one pulsatile cycle is 0.6 second. There are four exits in the aortic FE model. The flow rate is divided among the four exits based on the physiology of an average human being. The realistic outflow rates are is 7 % for left subclavian, 10 % for left common carotid arteries 7 % for brachycephalic trunk and rest of the volume flows through descending aortic outlet. The total flow rate assumed is 6 l/m. Initial conditions include zero velocity components and pressure.

9.4 Results and discussions

In this artery, due to the presence of 180^0 bend, centrifugal effect influences the wall shear stress and pressure distributions. The three branches present in the aortic arch will also influence the flow pattern. The output quantities chosen to explain the response of the aneurysm to pulsatile haemodynamics are haemodynamical pressure, wall shear stress and oscillatory shear index. The importance of these haemodynamical quantities has already been explained in the Chapter 3. Pressure distribution plots at two instances are given in Figure 9.4. WSS plots for two selected time steps can be found in the Figure 9.5. In order to capture the flow behavior, the instances chosen are start of the pulse, peak systole, early systolic deceleration, end systole deceleration and a diastolic step. The Figure 9.6 shows the variation of WSS with time. The anterior and posterior views of OSI distribution in the aorta are shown in the Figure 9.7.

9.4.1 Haemodynamic pressure in the aorta

Haemodynamical pressure is the primary load on the aneurysmal wall, thus it is one of the factors responsible for pathogenesis and rupture of aneurysm [16]. The blood pressure creates

Table 9.1: TAA: Harmonics used to generate unsteady velocity profile.

Harmonic	Frequency (Hz)	Amplitude	Phase (rad)
0	0.000	126.88125	0.0000
1	1.63548	219.048	-1.6
2	3.27097	156.0645	3.049
3	4.90645	80.25450	1.813
4	6.5419	57.644	1.224
5	8.17742	56.193	-0.10786
6	9.81290	25.001	-1.55024
7	11.44840	17.105	-1.405
8	13.08390	24.24746	-2.9386
9	14.71940	8.16	1.4578
10	16.35480	10.9	2.745
11	17.99030	12.68	0.49
12	19.62580	2.756	-2.4845
13	21.2613	5.98	-0.25438

(a) Pressure plot in the second systolic (2nd time step) step.

(b) Pressure plot at early systolic (7th time step) deceleration.

Figure 9.4: Pressure distribution in the Aorta.

a normal force on the endothelial wall, which is tensile in nature. In the beginning of the pulse (Figure 9.4a), the pressure value decreases gradually, starting from the upstream-aortic inlet to the downstream-aortic outlet. This pattern is same as those of idealised arteries in the previous chapters (at lower Re only). At peak systole (Figure not shown here), peak pressure occurs in the aortic arch, since centrifugal effect due to peak velocity impinges the fluid particles on the external curvature of the aortic arch. During the early systolic deceleration (Figure 9.4b) and late systolic deceleration, the peak pressure is occurring on aneurysmal wall. This high pressure zone might be susceptible for rupture initiation. The deceleration and flow reversal

of the blood causes the pressure drop to switch from outlet to inlet. The value of the haemodynamic pressure on the aneurysmal wall at late systolic deceleration step is 64.0 dynes/cm^2. At the diastolic step (Figure not shown here), the pressure drop completely reverses, with zero pressure at the inlet and peak pressure at the outlet.

(a) WSS in the second systolic step-Anterior view. (b) WSS at late (18th time step) systolic deceleration-Posterior view

Figure 9.5: Wall shear stress in the aorta.

9.4.2 Wall shear stress in TAA

The location of peak wall shear stress and its value have shown strong dependence on time. Folded neck is found to be the most affected region by WSS, since the fluid particles shear with the sharp bend. At the beginning of the pulsatile flow, peak WSS (Figure 9.5) occurs at the folded neck. However the value of peak WSS is found to be small (90 dynes/cm^2). For the peak systolic acceleration and early systolic deceleration steps, location of peak WSS (Figures not shown here) remains at the folded neck. The peak WSS in the folded neck reaches as high as 415 dynes/cm^2 at the peak systolic acceleration step. Whereas, for the aorta without folded neck, the peak WSS is found to be as low as 200 dynes/cm^2 (in the location where there was folded neck). At the diastolic step, the peak WSS is concentrated at two locations (Figure not shown here). These two locations are the bend region (65 dynes/cm^2) of ascending aorta and a location (62 dynes/cm^2) proximal to the aneurysm. The WSS concentration at these two location occurs, since the decelerating fluid particles shear with the bent walls. At the diastolic step, for the aorta without folded neck, peak WSS (50 dynes/cm^2) occurred at a location in the bend region of ascending aorta. WSS in the aneurysm remains low (less than 10 dynes/cm^2) for all the 99 steps. The variation of the WSS with respect to time has been given in Figure 9.6. From the figure it is clear that, the peak WSS occurring at the peak systolic flow is 400 dynes/cm^2. This value is higher than the yield stress for endothelial wall, suggested by *Fry* [52]. *Fry* [78] has also suggested that, a WSS value as high as 800 dynes/cm^2 can erode endothelial cells. According to the Figure 9.6, the WSS is proportional to the flow velocity until the late systole. But, from the late systole to early diastole, the WSS fluctuates. This fluctuation is due to the reversed flow and forward moving flow.

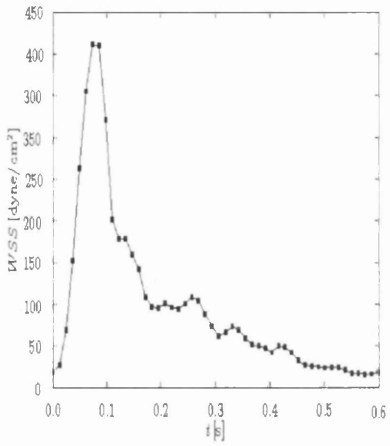

Figure 9.6: TAA: Peak WSS vs time.

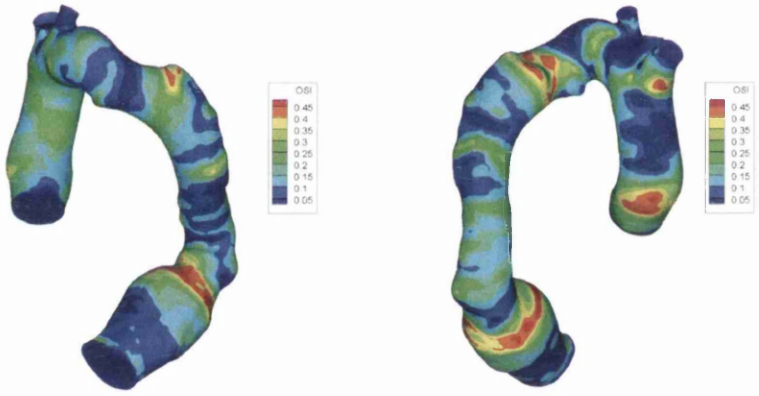

(a) Anterior view (b) Posterior view

Figure 9.7: TAA: Oscillatory Shear Index in the aorta.

9.4.3 Oscillatory shear index in TAA

The definition and equation of dimensionless OSI are given in the Section 3.5. From the Figure 9.7, it is evident that, the peak OSI is located proximal to the aneurysm. But the WSS is very low (for all the time steps) at this region. This proves that, the combination of higher OSI and lower WSS is responsible for pathogenesis of aneurysm. Higher OSI can also be located in the beginning of ascending aorta, outlet to brachycephalic artery and the start of descending aorta. These locations are subjected to multidirectional and fluctuating shear stresses. The maximum possible value of OSI is 0.5. The maximum OSI found in the aorta is 0.49, which is occurring at a location proximal to aneurysm. Higher OSI at this particular location, suggests higher residence time [79] of blood particles and increased permeability of endothelium to low density lipoprotein (LDL).

Chapter 10

Conclusions and Future scope

10.1 Conclusions

Initially, a brief introduction to blood circulation, arteries and hemodynamics has been presented. Governing equations of blood flow and an efficient solution scheme to them have been discussed. The characteristic based split-solution scheme discussed here, is found to be suitable for bio-fluid dynamical problems. Steady flow through four idealistic arteries has been presented. Pulsatile flow through a realistic artery has also been explained. Flow through a straight artery has been validated with analytical calculations. The validation is in good agreement and supports the idea of implementing numerical simulation in diagnosis and treatment of vascular pathologies. Flow pattern in the straight artery is found to be smooth, with no flow disturbances and no stronger secondary flow. Whereas the presence of bends in an artery disturbs the flow. Presence of bend also increases the pressure drop and wall shear stress. In the artery with a single bend, at higher Reynolds number, peak pressure occurs at the external curvature of the bend. In the single bend artery, recirculation in the plane of cross-section occurs downstream only and secondary flow becomes complex at higher Reynolds number. Second problem solved, involves two bends in the artery. In this double bend artery, flow in the second bend differs significantly from the flow in first bend. Flow in the second bend is highly dependent on Reynolds number. In the second bend, the location of maximum axial velocity shifts to the opposite wall at higher Reynolds number. No recirculation occurs in the first bend, whereas four vortices have been observed in the second bend. Third problem solved also involved two bends, but the angle of curvature is higher. The increase in angle of curvature increases the pressure drop drastically, whereas variation in WSS is found to be ignorable. In the Chapter 8, the artery with same angle of curvature has been solved for two lumen radii. The location of peak WSS is found to vary with lumen radius. Strength of secondary flow varies with lumen radius at a given Reynolds number. Pressure drop and WSS decrease with increase in lumen radius. In all the bend-type problems, relatively lower WSS has been found in internal curvatures. This fact suggests that, internal curvatures are vulnerable for atherogenesis and lesion formation. Finally, pulsatile flow through an aorta inflicted with thoracic aortic aneurysm has been elucidated. The aorta consists of a rare geometrical feature, which is a folded neck. In this chapter, a brief introduction to aneurysm, and their pathogenesis and diagnosis has been explained. The haemodynamical discussion in this chapter also involves geometrical and numerical modeling of TAA. The spatial and temporal distribution of haemodynamical quantities such as WSS and pressure on the aortic wall has been discussed. Temporally, peak wall

shear stress and its location is found to vary significantly with inlet velocity. For most of the time steps, higher WSS occurs at the folded neck. WSS is found to be low on and around the aneurysmal wall for all the time steps. Oscillatory shear index is found be high at a location proximal to aneurysmal wall. This supports the fact that, low WSS and high OSI could be responsible for pathogenesis of aneurysm. Numerical simulation has also been performed on an aorta without sharp-folded neck. In this case peak WSS is found to be half of that of the realistic aorta.

10.2 Future Scope

This research work can be extended in numerous directions. The work to consider pulsatile inlet flow conditions to the bend artery is underway. In this study, it is expected to locate higher OSI in the internal curvatures. The work done here on bend type arteries can also be proceeded towards out of plane bend-type arteries. Little or no literature exists in these type of idealized arteries. In the future, arteries with more than two bends should be studied. Strength of secondary flow is highly dependent on number bends. Many regions with flow separation are expected to arise, with increase in number of bends. Multiple bends are common geometrical features of femoral arteries [19]. The effect of angle of curvature of the bend on the flow should be studied thoroughly by considering many angles. The effect of radius of curvature should also be studied on arteries. There is a need to study other types of idealized arteries using CBS-AC scheme. These arteries can be carotid bifurcation or cerebral arteries. Presence of bifurcation in the carotid is expected to have greater impact on WSS and OSI patterns. The realistic model of TAA should be studied using realistic inlet and outlet velocity profiles. The realistic velocity profiles are expected to be asymmetric rather than fully developed. It is very important to include wall distensibility, thus the idealistic and realistic arteries should be restudied by considering the deformation of wall.

Bibliography

[1] B.K. Bharadvaj, R.F. Mabon and D.P. Giddens. Steady flow in a model of the human carotid bifurication. Part1-Flow visualization. *Journal of Biomechanics*, 1982;15:349-362.

[2] A.A. van Steenhoven, F.N. van de Vosse, C.C.M. Rindt. Experimental and numerical analysis of carotid artery blood flow. *Blood Flow in Large Arteries:Applications and Clinical Medicine*, 1990;15:250-260.

[3] Toshihisa Asakura and Takeshi Karino. Flow patterns and spatial distribution of atherosclerotic lesions in human coronary arteries. *Circulation Research*, 1990;66:1045-1066.

[4] Spiros G. Frangos, MD; Vivian Gahtan, MD; Bauer Sumpio, MD, PhD. Localization of atherosclerosis:Role of hemodynamics. *Archives of Surgery*, 1999;134:1142-1149.

[5] David N. Ku and Don P. Giddens. Pulsatile flow in a model carotid bifurcation. *Atherosclerosis*, 1983;3:31-39.

[6] Peter F. Davies. Mechanisms involved in endothelial responses to hemodynamic forces. *Atherosclerosis*, 1997;131:S15-S17.

[7] W.E. Stehbens. Turbulence of blood flow. *Experimental Physiology*, 1958;44:111-118.

[8] George S.K. Fung, S.K. Lam, Stephen W.K. Cheng, K.W. Chow. On stent-graft models in thoracic aortic endovascular repair:A computational investigation of the hemodynamic factors. *Computers in Biology and Medicine*, 2008;38:484-489.

[9] Bok Y. Lee, M.D., Cyrus Assadi, M.D., John L. Madden, M.D., David Kavner, D.Eng., Frieda S. Trainor, Ph.D., and William J. McCann, M.D. Hemodynamics of arterial stenosis. *World Journal of Surgery*, 1978;2:621-629.

[10] John D. Anderson, Jr. *Computational Fluid Dynamics*, McGraw-Hill international editions, 1995.

[11] Y.C. Fung. *Biomechanics:Circulation*. Spring-Verlag, 1997.

[12] C.A.J Fletcher. *Computational Techniques for Fluid Dynamics 1*, Spring-Verlag, 1988.

[13] P. Nithiarasu, R. Codina and O. C. Zienkiewicz. The Characteristic based split (CBS) scheme-a unified approach to fluid dynamics. *International Journal for Numerical Methods in Engineering*, 2006;66:1514-1546.

[14] P. Nithiarasu. An efficient artificial compressibility (AC) scheme based on the characteristic based split (CBS) method for incompressible flows. *International Journal for Numerical Methods in Engineering*, 2002;56:1815-1845.

[15] J.R. Womersley. Method for the calculation of velocity, rate of flow and viscous drag in arteries when pressure gradient is known. *Journal of Physiology*, 1955;127:553-563.

[16] Yannis Papaharilaou and John A. Ekaterinaris. The Influence of asymmetric inflow in abdominal aortic aneurysm hemodynamics. *P. Wesseling et al*, editor, *European Conference on Computational Fluid Dynamics*, Delft, The Netherlands, 2006.

[17] M.J. O'Rourke and J.P. McCullough. A comparison of the measured and predicted flow-field in a patient-specific model of an abdominal aortic aneurysm. *Journal of Engineering in Medicine*, 2008;222:737-750.

[18] Charles L. Feldman, Jesse S. Fernandes, Peter H. Stone. Flow imaging of 3-dimensional coronary artery models using computational Fluid Dynamics - Effet of Coronary Artery Curvature. *IEEE*, 1993;93:775-777.

[19] H.W. Hoogstraten, J.G. Kootstra, B. Hillenb, J.K.B. Krijgerb and P.J.W. Wensing. Numerical simulation of blood flow in an artery with two successive bends. *Journal of Biomechanics*, 1996;29:1075-1083.

[20] N.B. Wood, S.Z. Zhao, A. Zambanini, M. Jackson, W. Gedroyc, S.A. Thom, A.D. Hughes, and X.Y. Xu. Curvature and tortuosity of the superficial femoral artery:a possible risk factor for peripheral disease. *Journal of Applied Physiology*, 2006;101:1412-1418.

[21] Zurong Ding, Keqiang Wang, Jie Li, Xushwn Cong. Flow field and oscillatory shear stress in a tuning-fork-shaped model of the average human carotid bifurication. *Journal of Biomechanics*, 2001;34:1555-1562.

[22] D. Lee, J.Y. Chen. Numerical simulation of steady flow fields in a model of abdominal aorta with its peripheral branches. *Journal of Biomechanics*, 2002;35:1115-1122.

[23] J. Peraire, M. Vahdati, K. Morgan and O.C. Zienkiewicz. Adaptive remeshing for compressible flow computations. *Journal of Computational Physics*, 1987;72:449-466.

[24] A.K. Qiao, X.L. Guob, S.G. Wub, Y.J. Zeng, X.H. Xua. Numerical study of nonlinear pulsatile flow in S-shaped curved arteries. *Medical Engineering and Physics*, 2004;26:545552.

[25] Chain-Nan Yung, Kenneth J. Dewitt, Srikanth Subramanian, Abdollah A. Afjeh, Theo G. Keith. Three-dimensional pulsatile flow through a bifurication. *IEEE*, 1996;26:106109.

[26] Jens D. Muller, Maiki Jitsumura. Sensitivity of flow patterns in cerebral aneurysms. In P. Nithiarasu and R. Lohner, Editors *Proceedings:1st International Conference on Mathematical and Computational Biomedical Engineering-CMBE2009*, Swansea, UK.

[27] G. Houzeaux, R. Aubry, M. Vazquez, and H. Calmet. Large-scale CFD in cerebral hemodynamics:Charecterizing arterial flow. In P. Nithiarasu and R. Lohner, Editors *Proceedings:1st International Conference on Mathematical and Computational Biomedical Engineering-CMBE2009*, Swansea, UK.

[28] Juan R. Cebral, Marcelo A. Castro, James E. Burgess, Richard S. Pergolizzi, Michael J. Sheridan, and Christopher M. Putman. Characterization of cerebral aneurysms for assessing risk of rupture by using patient-specific computational hemodynamics Models. *American Journal of Neuroradiology*, 2005;26:25502559.

[29] Paul Sutton. *Cardiovascular System*, Mosby-Elsevier, 2008.

[30] Mario Bassini, Ph.D., Emilio Gatti, Ph.D., Tito Longo, M.D., Gianmarco Martinis, Ph.D., Paolo Pignoli, M.D., Pier Luigi Pizzolati, Ph.D.. *In Vivo* recording of blood velocity profiles and studies *In Vitro* of profile alterations induced by known stenoses. *Texas Heart Institute Journal*, 1982;9:185192.

[31] A. Rabiee, A.N. Ziaei, M.M. Alishahi and H. Emdad. A robust algorithm for computing fluid flows on highly non-smooth staggered grids. *International Journal For Numerical Methods in Fluids*, 2009;59:10111033.

[32] H.E. Fiedler. A note on secondary flow in bends and bend combinations. *Experiments in Fluids*, 1997;23:262264.

[33] Peter Tibaut, Bruno Wiesler, Michael Mayer, Rainer Wegenkittel. Blood flow in vessels with artificial or pathological geometrical changes. *Biomedicine*, 2-4 April 2003, Ljubljana, Slovenia.

[34] J.P. Mynard and P. Nithiarasu. A 1D arterial blood flow model incorporating ventricular pressure, aortic valve and regional coronary flow using locally conservative galerkin method. *Communications in Numerical Methods in Engineering*, 2008;24:367417.

[35] Peter Vennemann, Ralph Lindken and Jerry Westerweel. *In vivo* whole-field blood velocity measurement techniques. *Exp Fluids* 2007;42:495511.

[36] Xiaoyi He, David N. Ku, and James E. Moore, Jr. Simple calculation of the velocity profiles for pulsatile flow in a blood vessel using mathematica. *Annals of Biomedical Engineering*, 1993;21:4549.

[37] David F. Moore, Gheona Altarescu, Randall Pursley, Umberto Campia, Julio A. Panza, Emilios Dimitriadis and Raphael Schiffmann. Arterial wall properties and Womersley flow in fabry disease. *BMC Cardiovascular Disorders*, 2002;1471-2261.

[38] Marc Thiriet. *Biology and Mechanics of Blood Flows:Part2*, Springer, 2008.

[39] Marc Thiriet. *Biology and Mechanics of Blood Flows:Part1*, Springer, 2008.

[40] Oguz Kerim Baskurt. Pathophysiological significance of blood rheology. *Turkish Journal of Medical Sciences*, 2003;33:347355.

[41] G.B. Thurston. Viscoelasticity of blood. *Biophysical Journal*, 1972;12:12071218.

[42] Amy G. Tsai, Cesar Acero, Patricia R. Nance, Pedro Cabrales, John A. Frangos, Donald G. Buerk, and Marcos Intaglietta. Elevated plasma viscosity in extreme hemodilution increases perivascular nitric oxide concentration and microvascular perfusion. *The American Physiological Society*, 2004;288:17301740.

[43] D.S. Sankar and K. Hemalathab. A non-Newtonian fluid flow model for blood flow through a catheterized arterySteady flow. *Applied Mathematical Modelling*, 2007;31:18471864.

[44] Paul F. Fischera, Francis Loth, Seung E. Leec, Sang-Wook Leed, David S. Smith and Hisham S. Bassiounye. Simulation of high-Reynolds number vascular flows. *Computer Methods in Applied Mechanics and Engineering*, 2007;196:30493060.

[45] Philip I. Aaronson and Jeremy P. I. Ward. *The Cardiovascular System at a Glance*, Blackwell publishing, 2007.

[46] J. Rodney Levick. *An Introduction to Cardiovascular Physiology*, Hodder Arnod, 2003.

[47] Lee Waite and Jerry Fine. *Applied Biofluid Mechanics*, McGrawhill, 2003.

[48] Mahmud Ashrafizaadeh and Hani Bakhshaei. A comparison of non-Newtonian models for lattice Boltzmann blood flow simulations. *Computers and Mathematics with Applications*, 2009;58:10451054.

[49] Cheng-Maw Ho, Shun-Feng Tsai, Reui-Kuo Lin, Po-Chin Liang, Tony Wen-Hann Sheu, Rey-Heng Hu, Po-Huang Lee. Computer simulation of hemodynamic changes after right lobectomy in a liver with intrahepatic portal vein aneurysm. *Journal of Formos Medical Association*, 2007;106:617624.

[50] Shakil Ahmed, Ilija D. Sutalo and Helen Kavnoudias. Hemodynamics and stress disyribution in a cereberal aneurysm partially blocked with coils. *Fifth International Conference on CFD in the Process Industries-2006*, CSIRO, Melbourne.

[51] O. Smedby, J. Johansson, J. Molgaard, A.G. Olsson, G. Walldius, U. Erikson. Predilection of atherosclerosis for the inner curvature in the femoral artery. *Arteriosclerosis, Thrombosis, and Vascular Biology*, 1995;15:912-917.

[52] Donald L. Fry, Acute vascular endothelial changes associated with increased blood velocity gradients. *Circulation Research*, 1968;22:165197.

[53] Rodkiewicz C.M., Vishwanath N., And Zajac S. On the abdominal aneursyms-Numerical and *in vitro* experimental study. *RC IEEE-EMBS and 14th MESL*, September-1995.

[54] A.G. Radaelli, L. Augsburgerber, J.R. Cebral, M. Ohta, D.A. Rufenacht, R. Balossino, G. Benndorf, D.R. Hose, A. Marzoh, R. Metcalfe, P. Mortier, F. Mut, P. Reymond, L. Socci, B. Verhegghe, A.F. Frangi. Reproducibility of haemodynamical simulations in a subject-specific stented aneurysm model-A report on the Virtual Intracranial Stenting challenge 2007. *Journal of Biomechanics*, 2008;41:20692081.

[55] Stephen C. Nicholls, MD, David J. Phillips, PhD Jean F. Primozich, BS, Ramona L. Lawrence, BS, Ted R. Kohler, MD, Thomas G. Rudd, MD, and D. Eugene Strandness Jr., MD. Diagnostic significance of flow separation in the carotid bulb. *Stroke:Journal of american heart association*, 1989;20:175182.

[56] H.J. Ralston and A.N. Taylor. Streamline flows in the arteries of the dog and cat. *American Journal of Physiology*, 1945;144:706710.

[57] H.N. Sabbah, E.T. Hawkins and P.D. Stein. Flow separation in the renal arteries: *Arteriolisis, Thrombosis, and Vascular Biology*, 1984;4;28-33.

[58] A.P. Yoganathan, Fluid mechanics of aortic stenosis. *European Heart Journal*, 1988;9;13-17.

[59] Taedong Kim, Taewon Seo, and Abdul I. Barakat. Numerical simulations of fluid mechanical interactions between two abdominal aortic branches. *Korea-Australia Rheology Journal*, 2004;16;75-83.

[60] Robert S. Reneman, Theo Arts, Arnold P. Hoeks. Wall shear stressan important determinant of endothelial cell function and structure in the arterial system *in vivo*. *Journal of Vascular Research*, 2006;43:251269.

[61] Masaaki Shojima, MD; Marie Oshima, PhD; Kiyoshi Takagi, MD, PhD; Ryo Torii, PhD; Motoharu Hayakawa, MD, PhD; Kazuhiro Katada, MD, PhD;Akio Morita, MD, PhD; Takaaki Kirino, MD, PhD. Computational fluid dynamic study of 20 middle cerebral artery aneurysms. *Stroke:Journal of American Heart Association*, 2004;35;2500-2505.

[62] David N. Ku, Don P. Giddens, Christopher K. Zarins, and Seymour Glagov. Pulsatile flow and atherosclerosis in the human carotid bifurcation. *Arteriosclerosis*, 1985;5:293-302.

[63] D. Lee, J.Y. Chen. Pulsatile flow field in a model of abdominal aorta with its peripheral branches. *Biomedical Engineering-Application,Basis and Communications*, 2003;15:170-178.

[64] A.D. Augst, D.C. Barratt, A.D. Huges, S.A. McG Thom and X.Y. Xu. Various issues relating to computational fluid dynamics simulation of carotid bifurcation flow based on models reconstructed from three-dimensional ultrasound images. *IMechE2003*, 2003;217:393-403.

[65] Jaques S. Milner, Jennifer A. Moore, Brian K. Rutt and David A. Steinman. Hemodynamics of human carotid artery bifurcations:Computational studies with models reconstructed from magnetc resonsance imaging of normal subjects. *Journal of Vascular Surgery*, 1998;27:143-156.

[66] A.S. Yang, C.Y. Wen and L.Y. Tseng. *In vitro* characterization of aortic flow using numerical simulation, phase-contrast magnetic resonance imaging, and particle tracking images. *IMechE*, 2008;222:2455-2462.

[67] Tong-Miin Liou, Yi-Chen Li, Wei-Cheng Jaun. Numerical and experimental studies on pulsatile flow in aneursyms arising laterally from a curved parent vessel at various angles. *Journal of Biomechanics*, 2007;40:1268-1275.

[68] Zhao Jun-wei, Yin Wen-yi, Ding Guang-hong. Numerical simulation and analysis on the the hemodynamics of an elastic aneurysm. *Journal of Hydrodynamics*, 2008;20(2):216-224.

[69] Don R. Wells, Joseph P. Archie,Jr., and Clement Kleinstreuer. Effect of carotid artery geometry on the magnitude and distribution of wall shear stress gradients. *Journal of Vascular Surgery*, 1996;23:667-678.

[70] Chorin A.J. A Numerical method for solving incompressible viscous flow problems. *Journal of Computational Physics*, 1967;2:12-26.

[71] M.M. Thompson and P.R.F Bell. ABC of arterial and venous disease:Arterial aneurysms. *British Medical Journal*, 2000:320(7243): 11931196.

[72] Christoph Engelke, Aarthi R. Mohan, Tarun Sabharwal, John F. Reidy. Peripheral aneurysm rupture in a patient with inactive systemic lupus erythematosus. *European Radiology:Vascular Intervention*, 2002:12:28952897.

[73] D. Wang, O. Hassan, K. Morgan and N. Weatherill. EQSM: An efective high quality surface grid generation method based on remeshing. *Comput. Methods Appl. Meth. Engrg*, 2006:195:5621-5633.

[74] Igor Sazonov, Prihambodo H. Saksono, Perumal Nithiarasu, Raoul van Loon, Heyman Luckraz and Saeed Ashraf. EQSM: Patient-specific blood flow simulation through an aneurysmal thoracic aorta with a folded neck. *Communication in Numerical Methods in Engineering*, 2003:00:1-6.

[75] Richard A. Malinauskas, Pasha Sarraf, Kevin M. Barber, George A. Truskey. Association between secondary flow in models of the aorto-celiac junction and subendothelial macrophages in the normal rabbit. *Atherosclerosis*, 1998:140:121-134.

[76] Richard A. Malinauskas, Robert A. Herrmann, George A. Truskey. The distribution of intimal white blood cells in the normal rabbit aorta. *Atherosclerosis*, 1994:115:147-163.

[77] R.K. Banerjee, Y.I. Cho and L.H. Back. Numerical studies of three-dimensional arterial flows in reversed curvature geometry:Part I-peak flow. *Journal of Biomechanical Engineering*, 1993:115:316-326.

[78] Donald L. Fry. Certain histological and chemical responses of the vascular interface to acutely induced mechanical stresses in the aorta of the dog. *Circulation Research*, 1969;24:93108.

[79] Heather A. Himburg, Deborah M. Grzybowski, Andrew L. Hazel, Jeffrey A. LaMack, Xue-Mei Li, and Morton H. Friedman. Spatial comparison between wall shear stress measures and porcine arterial endothelial permeability. *Am J Physiol Heart Circ Physiol*, 2003;286:H1916-H1922.

[80] R.L.T. Bevan, P. Nithiarasu, R. VanLoon and I. Sazonov, H. Luckraz and A. Granham, Application of a locally conservative Galerkin (LCG) method for modelling blood flow through a patient-specific carotid bifurcation, *International Journal for Numerical Methods in Fluids*, to appear in 2010

[81] Kent M Van De Graaff . *Human Anatomy*, McGraw-Hill international editions, 1998.

UNIVERSITY OF WALES SWANSEA LIBRARY